Uncovering cryptic pockets in the SARS-CoV-2 spike glycoprotein

Lorena Zuzic,[1,2,†] Firdaus Samsudin,[1,†] Aishwary T. Shivgan,[1] Palur V. Raghuvamsi,[3] Jan K. Marzinek,[1] Alister Boags,[1,4] Conrado Pedebos,[4,5] Nikhil K. Tulsian[3,6], Jim Warwicker,[7] Paul MacAry[8], Max Crispin,[9] Syma Khalid,[4,5,*] Ganesh S. Anand[3,10,*] and Peter J. Bond[1,3,‡,*]

[1]Bioinformatics Institute (A*STAR), Singapore 138671, Singapore
[2]Department of Chemistry, Faculty of Science and Engineering, Manchester Institute of Biotechnology, The University of Manchester, Manchester M1 7DN, United Kingdom
[3]Department of Biological Sciences, National University of Singapore, Singapore 117543, Singapore
[4]School of Chemistry, University of Southampton, Southampton SO17 1BJ, United Kingdom
[5]Department of Biochemistry, University of Oxford, Oxford OX1 3QU, United Kingdom
[6]Department of Biochemistry, National University of Singapore, Singapore 117546, Singapore
[7]School of Biological Sciences, Faculty of Biology, Medicine and Health, Manchester Institute of Biotechnology, The University of Manchester, Manchester M1 7DN, United Kingdom
[8]Life Sciences Institute, Centre for Life Sciences, National University of Singapore, 28 Medical Drive, Singapore 117546, Singapore
[9]School of Biological Sciences, University of Southampton, Southampton SO17 1BJ, United Kingdom
[10]Department of Chemistry, The Pennsylvania State University, University Park, PA 16802, United States of America

[†]These authors contributed equally to the paper
[‡]Lead contact

*To whom correspondence should be addressed:
E-mail: peterjb@bii.a-star.edu.sg **(Lead Contact)**
E-mail: gsa5089@psu.edu
E-mail: s.khalid@soton.ac.uk

Summary

The COVID-19 pandemic has prompted a rapid response in vaccine and drug development. Herein, we modelled a complete membrane-embedded SARS-CoV-2 spike glycoprotein and used molecular dynamics simulations with benzene probes designed to enhance discovery of cryptic pockets. This approach recapitulated lipid and host metabolite binding sites previously characterised by cryo-electron microscopy, revealing likely ligand entry routes, and uncovered a novel cryptic pocket with promising druggable properties located underneath the 617-628 loop. A full representation of glycan moieties was essential to accurately describe pocket dynamics. A multi-conformational behaviour of the 617-628 loop in simulations was validated using hydrogen-deuterium exchange mass spectrometry experiments, supportive of opening and closing dynamics. The pocket is the site of multiple mutations associated with increased transmissibility found in SARS-CoV-2 variants of concern including Omicron. Collectively, this work highlights the utility of the benzene mapping approach in uncovering potential druggable sites on the surface of SARS-CoV-2 targets.

Introduction

The rapidly spreading outbreak of COVID-19 caused by a novel coronavirus, SARS-CoV-2 (Gorbalenya et al., 2020), has triggered an unprecedented scale of global socioeconomic meltdown (Wu et al., 2020). SARS-CoV-2 is a large enveloped single-stranded RNA virus with a helical nucleocapsid and with a characteristic crown-like halo of viral envelope proteins. Central to the mechanism of infection is the spike (S) protein on the surface of the virion, which is the primary target for vaccine and therapeutics development. The S protein is a class I viral fusion protein trimer composed of two major subunits: S1, which facilitates host cell recognition by interacting with the human angiotensin converting enzyme 2 (ACE2), and S2, which mediates membrane fusion and entry into the host cell. To date, several structures of the prefusion S protein ectodomain (ECD) and its receptor binding domain (RBD) bound to ACE2 have been resolved using cryo-electron microscopy (cryo-EM) and X-ray crystallography (Cai et al., 2020; Lan et al., 2020; Walls et al., 2020; Wrapp et al., 2020; Wrobel et al., 2020; Yan et al., 2020). The S protein is a large trimeric protein made of various functional domains, densely covered with glycans (Watanabe et al., 2020), and it is structurally divided into two distinctive regions: a club-shaped head and a flexible stalk (Figure 1A). The two dominant conformations of the S protein chains involve the RBD in an ‘up’ state, which renders the S protein competent for receptor binding, and a 'down’ state, which has inaccessible ACE2-binding surfaces. The S protein is open if any of the three chains are in an ‘up’ conformation; otherwise, the S protein cannot bind to the ACE2 and is therefore considered closed.

During the course of the pandemic, mutants with a D614G substitution on the S protein rapidly outcompeted other strains. The mutation is now an important feature of all SARS-CoV-2 variants of concern as it is linked to higher rates of transmission compared to the D614 wild type (WT) variant (Korber et al., 2020). Disruption of the D614-K854 salt bridge and accompanying structural changes in the S protein lead to better conformational sampling of open states (Yurkovetskiy et al., 2020). Additionally, the point mutation stabilises the S1:S2 complex and thus prevents premature dissociation of the S1 domain, allowing more S proteins to interact with the host receptor (Zhang et al., 2021). The S1:S2 stabilisation is linked to ordering of a 620-640 loop, which wedges itself into a gap lined with hydrophobic residues located between an N-terminal domain (NTD) and a C-terminal domain 1 (CTD1) (Figure 1A). In D614 WT, this loop is largely disordered. The same loop is linked to multimerisation events, where it extends and inserts into the NTD of a neighbouring S protein, effectively forming higher-order structures consisting of two or three S protein components (Bangaru et al., 2020). Structural and biophysical studies along with molecular dynamics (MD) simulations have shown that the S protein is highly dynamic (Casalino et al., 2020; Ke et al., 2020; Raghuvamsi et al., 2021; Turoňová et al., 2020). Crucially, several cryo-EM structures have uncovered cryptic pockets in the RBD and NTD, which serve as potential druggable epitopes (Bangaru

et al., 2020; Carrique et al., 2020; Toelzer et al., 2020). Linoleic acid (LA) was observed in the cryptic pocket of the RBD from which it also forms stabilising interactions with the RBDs of neighbouring chains (Toelzer et al., 2020). The presence of LA in the binding pocket shifts the S protein equilibrium towards closed conformations, which also has an effect on reduced ACE2 binding *in vitro*. Rational drug design approaches have been directed towards the LA pocket with the aim of stabilising receptor binding-incompetent closed conformations (Ellis et al., 2021; Shoemark et al., 2021). It appears that the LA pocket also has long-range effects on allosteric networks that include neighbouring chains, NTD, and distant S1/S2 cleavage sites (Oliveira et al., 2021; Tan et al., 2022). The NTD contains a cryptic site that binds a polysorbate (PS) detergent molecule if it is present in vaccine formulation (Bangaru et al., 2020; Ma et al., 2021). The same pocket can accommodate haem metabolites biliverdin and bilirubin, the presence of which change the NTD epitope presentation and modulate the antibody response (Rosa et al., 2021a).

Long timescale MD simulations performed on exascale computers have also discovered the existence of numerous cryptic epitopes across the viral proteome (Zimmerman et al., 2021). In recent years, simulations of therapeutically relevant proteins with small organic probes have successfully been used to induce energetically unfavourable opening of hydrophobic cryptic pockets and subsequently identify novel druggable sites (Kuzmanic et al., 2020; Sayyed-Ahmad and Gorfe, 2017; Tan and Verma, 2020). In this work, we thus built a membrane-bound glycosylated model of the S protein and simulated it in the presence of a solution containing benzene probes, to enhance the sampling of novel cryptic pockets that could potentially be targeted by small molecules, peptides, or monoclonal antibodies. Our study not only recapitulates cryptic pockets previously characterised by cryo-EM, but also identifies a novel pocket with promising druggable properties.

Results

Spike model validation

We first built a full-length model of the S protein in the one-RBD-up open conformation using available structural and glycomics data (details in STAR Methods). Three different glycosylation patterns were generated: non-glycosylated S protein to represent the original state of the protein, oligomannose-type glycans on all 22 glycosylation sites to represent the unprocessed glycoform, and the most dominant glycans species based on liquid chromatography-mass spectrometry (LC-MS) glycomics data (Watanabe et al., 2020) to represent the final glycoform. To understand the behaviour of the S protein in its native environment, the model was then simulated in a model of the endoplasmic reticulum-Golgi intermediate compartment (ERGIC) membrane, where coronaviruses are assembled

(Klumperman et al., 1994; Krijnse-Locker et al., 1994). The list of simulations is provided in Table S1.

Interestingly, in all simulations the S protein did not maintain an upright conformation with respect to the plane of the membrane. Instead, we observed a tilting motion of the ECD of up to 90°, facilitated by the two flexible hinges between the ECD and HR2 domains as well as between the HR2 and transmembrane (TM) domains (Figure 1B and 1C). The flexible bending motion results in orientational freedom of the ECD, presumably yielding a more expansive sampling of the RBD at the host cell surface. This may potentially increase the probability of binding to the ACE2 receptor and hence contribute towards efficient virus-host cell recognition. Such structural dynamics are in good agreement with a range of experimental data including from hydrogen-deuterium exchange mass spectrometry (HDX-MS) (Raghuvamsi et al., 2021), cryo-EM of recombinant S protein ECD (Wrapp et al., 2020), and cryo-electron tomography (cryo-ET) of intact SARS-CoV-2 virions (Ke et al., 2020; Turoňová et al., 2020; Yao et al., 2020), as well as simulation studies of independently built S protein models (Casalino et al., 2020; Choi et al., 2021; Sikora et al., 2020). As expected, in simulations of the S protein modelled with either the predominant glycan species or oligomannose-type glycans, the glycans showed a high degree of mobility resulting in a larger surface area of the S protein being covered by them compared to what is observed in static structures (Figure 2). The glycans covered a larger percentage of the stalk surface compared to the ECD, in agreement with previous simulations (Casalino et al., 2020; Sikora et al., 2020). Collectively, the observed protein and glycan dynamics of our S glycoprotein models thus correlate well with other independent experimental and computational studies.

Benzene mapping recapitulates known cryptic pockets

We next set out to uncover cryptic binding pockets on the surface of the S glycoprotein that could potentially represent targets for rational drug design. Hence, we performed a series of 200 ns simulations of the membrane-embedded, full-length S protein models with a 0.2 M concentration of benzene molecules within the bulk solvent. The benzene parameters have been modified to prevent accumulation within the hydrophobic lipid environment (details in Methods) (Zuzic et al., 2020). This was confirmed by the low percentage of benzene found in contact with membrane lipids throughout the simulations, and a similar progression of area per lipid and membrane thickness compared to simulations without benzene, indicating that the presence of benzene did not alter the membrane environment (Figure S1A-C). The stable secondary structure of the whole S protein was preserved in simulations with benzene, and the backbone RMSD of the ECD was similar to control simulations, irrespective of glycoform, indicating that the overall assembly of the ECD was unaffected by the presence of benzene (Figure S1D-E). It should be noted that the trimeric coiled coils forming the HR2 domain

partially disintegrated as benzene accumulated at its interface (Figure S2A-C), likely because its trimeric interface is primarily composed of an array of hydrophobic residues (Figure S2D). A recent NMR study showed that the HR2 domain adheres transiently to the viral membrane during membrane fusion (Chiliveri et al., 2021). The hydrophobic residues around which benzene accumulated in our simulations, therefore, likely reflect the lipid binding surface. To examine if this structural disintegration affects the ECD, we performed a set of control simulations in the presence of 0.2 M benzene of the isolated ECD (without the HR2 and TM domains present) modelled in the dominant glycans state. The backbone RMSD progression and secondary structural preservation of the ECD from these control simulations were very similar to those from the equivalent full-length S protein simulations (Figure S3A-B). This suggests that changes in the structure of the HR2 domain caused by benzene aggregation does not have any detrimental structural impact upon the ECD. Due to the structural deviation of the HR2 domain, as well as the fact that the HR2 domain is more extensively covered by glycans, we therefore only consider cryptic pockets mapped onto the surface of the ECD of the S protein.

The differences between water-only and benzene simulations revealed multiple cryptic pockets on the surface of the S protein – two of which were previously known from structural studies and have hence been used here as positive controls – and one novel pocket located near the functionally interesting loop encompassing residues 617-628 (Figure 3). Our control ECD-only simulations revealed very similar apolar surface areas for all three pockets compared to simulations of full-length S protein, further corroborating that HR2 distortion does not impact the ECD (Figure S3C). We also detected pocket densities near a proposed binding site for bacterial lipopolysaccharide (Petruk et al., 2021), but because it is predominantly a surface groove, we have omitted it from further analysis (Figure S4).

PS pocket is stabilised in the presence of glycans

A PS detergent molecule has been observed to bind to the NTD when detergent was present in the formulation of the immunogen (Bangaru et al., 2020). The hydrophobic tail was embedded in the hydrophobic groove pointing towards the neighbouring chain, with the hydrophilic head more accessible to the protein surface. This site has also recently been shown to bind haem metabolites, which inhibits access to an antibody epitope on the NTD (Rosa et al., 2021b). The addition of benzene to the simulation system successfully uncovered the PS-binding pocket, even in the absence of PS (Figure 4A). The outline of the mapped pocket was also in agreement with the shape of the hydrophobic portion of the ligand, as confirmed via structural alignment (Figure 4B).

The upper edge of the PS pocket (residues 167-180) displayed opening and closing motions that affected the volume of the pocket cavity (Figure 4C, 4D). Notably, pocket opening

was greatly affected by the presence of benzene probes and glycans in the simulation system. PS pocket properties for dominant and mannose glycoforms in the presence of benzene closely reflected the pockets with experimentally bound PS and biliverdin ligands ($SASA_{exp}$ = 6.7 ± 0.4 nm^2; $SASA_{dom.gly,+bnz}$ = 6.5 ± 1.9 nm^2; $SASA_{mann.gly,+bnz}$ = 6.7 ± 2.0 nm^2; Figure 4A, 4C). In comparison, water-only simulations failed to generate pocket densities that matched the shape and properties of the ligand in question, with the pockets under those conditions exhibiting lower solvent accessibility ($SASA_{all,-bnz}$ = 4.0 ± 1.2 nm^2).

The systems without glycans displayed greater opening motions of the PS pocket upper edge (Figure 4C, 4D), suggesting that the absence of glycans results in an anomalous destabilisation of the PS pocket. The fully open pocket conformation was not sampled in glycosylated systems, implying that it is unlikely to be a relevant NTD conformational state. This example highlights the importance of explicit glycan consideration when addressing cryptic pocket properties. Glycan-mediated stabilisation may be particularly important in the context of benzene mapping, where the protein conformation is affected by the presence of hydrophobic probes.

LA pocket simulations reveal a common route for ligand entry

A second positive control verifying our method was the LA binding site, which has been shown to exist in the RBD in multiple cryo-EM structures (Bangaru et al., 2020; Carrique et al., 2020; Toelzer et al., 2020), but was not present in the structural templates of our initial S models (Wrapp et al., 2020). We detected increased pocket density in systems with benzene and across all glycoforms. The acyl tail of the LA ligand was accommodated in its entirety in the pocket density, consistent with the nature of the hydrophobic benzene probe, whereas the portion of the pocket outlining the polar carboxylate group was not detected in our simulations. It has been proposed that the presence of LA in the RBD shifts the dynamics of the S protein towards the closed state, whereby all RBDs are in the down configuration (Toelzer et al., 2020), allowing for the interactions of the fatty acid headgroup with the neighbouring chain. As our system was modelled using the S protein ECD in the open state, it is conceivable that the arrangement of the RBDs was not able to fully reproduce the complete outline of the LA binding site that also encompasses the fatty acid carboxylate.

The LA pockets exhibited patterns of solvent exposure that were dependent on chain conformation (Figure 5A). Those located on the up-pointing RBD are highly solvent-accessible due to the fact that they are not shielded by neighbouring chains. On the other hand, the pockets located on the down RBDs displayed hydrophobic SASA values that were more similar to the LA pockets in cryo-EM structures with bound ligands ($SASA_{exp}$ = 2.9 ± 0.2 nm^2; $SASA_{down,+bnz}$ = 4.3 ± 1.60 nm^2; $SASA_{up,+bnz}$ = 6.4 ± 2.47 nm^2). Thus, the down-state RBD is expected to be a better descriptor of an LA-binding mode, even though benzene probes were

unable to fully reproduce the LA-mediated stabilisation of RBDs. Benzene inside the pocket predominantly interacted with aromatic residues Tyr365, Tyr369, and Phe377 (Figure 5B), whereas Tyr369 also served as a first point of contact for benzene entering the pocket (Figure S5). This entry site (consisting of Tyr369, Ala372, and Phe374) is pertinent to benzene, but is also a likely entry point for LA, as it is located on an exposed flexible loop that allows for ligand ingress. Conversely, the LA pocket on the upwards-facing RBD exhibited exaggerated solvent accessibility (Figure 5A) and multiple sites of ligand entry (Figure 5B, S5). Taking into account the fact that the LA ligand induces stabilization of the closed structure, this conformation is unlikely to be reflective of the stable LA-binding state. However, since the simulated 'up' pocket was open and accessible for benzene entry, this suggests that the ligand may initially bind to the upwards-facing RBD, but stabilise only the down-state conformation.

A novel cryptic pocket detected around 617-628 loop

Finally, we also detected a novel pocket with a partial cryptic character located on the side of the S protein, which we term the multimerisation (MM) pocket (Figure 6A). The majority of the pocket volume occupies a shallow surface groove in the interchain region of the S protein, while the cryptic component of the pocket is present in the smaller subsection located underneath the 617-628 loop. Although this short loop is missing from our cryo-EM structural template (Wrapp et al., 2020), it was predicted to adopt a predominantly helical structure. Additionally, this loop has been shown to be helical in the thermostable disulphide-stabilised S protein construct (Xiong et al., 2020). In cryo-EM structures of S protein with the D614G substitution, this loop forms a helix due to a wider gap between the NTD and CTD1, which correlates with the more open conformation of the D614G S protein (Zhang et al., 2021). The hydrophobic contacts between this loop and a neighbouring segment, CTD2, stabilize the cleaved form of the S protein by preventing premature S1 shedding. A cryo-EM structure of an S protein dimer-of-trimer (Bangaru et al., 2020) shows that this loop is involved in the formation of S protein multimers on the viral surface via its insertion into the NTD of the neighbouring S protein. The cryo-EM map of the S dimer-of-trimer complex shows one 617-628 loop from each trimer interacting with the neighbouring NTD, thus establishing two symmetrical points of contacts between the spikes. Interestingly, when involved in multimerisation, the loop is extended and exists as a random coil, instead of the predicted helix.

Apolar pocket SASA depended on chain conformation (up vs. down) and glycosylation content (Figure 6B). In particular, the absence of glycans resulted in a greater solvent exposure, which (similarly to the PS pocket) demonstrated the importance of glycans in pocket stabilisation. Glycan contact mapping also revealed contacts predominantly located on the outwards-facing portion of the 617-628 loop (Figure 6C). The conformations associated with

the MM protein in a “no glycans” system, albeit showing greater apolar SASA content, are less likely to be representative of the S protein in a biological context. Instead, it is apparent that reproducing accurate MM pocket properties in modelling studies demands explicit consideration of glycan moieties, as they interact with and modulate MM pocket exposure.

We then examined the behaviour of the loop via HDX-MS experiments carried out at 37 ℃ (details in Methods). The peptide (residues 617-632) encompassing the loop exhibited qualitative bimodality, with a major low exchanging deuterium exchange envelope and a minor higher exchanging envelope that reflects either an intrinsic conformational ensemble behaviour or intratrimer conformational heterogeneity, with a major lower exchanging population and minor, higher exchanging population in solution (Figure 7) (Englander et al., 1996; Narang et al., 2020). This bimodal distribution has been clearly observed in HDX-MS of Spike at 25 ℃ at a locus region spanning residues 626-636; Multiple peptides displayed bimodal mass spectra, attributed to reversible unwinding of the trimeric S protein (Costello et al., 2022).

We compared the loop dynamics observed via HDX-MS with our simulated systems and observed a comparable multimodality in the behaviour of the loop, or in this case, its associated peptide. Solvent accessibility of the simulated peptide reflected a similar pattern of behaviour, with a large population of states with lower solvent accessibility, and rarer occurrences of states with a more accessible peptide surface. Cluster analysis likewise shows that the peptide is in a helical state for ~90% of cumulative simulation time, but occasionally rearranges itself into less structured random coil states (Figure S6A).

Discussion

The observed conformational heterogeneity in loop behaviour, both in experiment and in simulation, may be of functional importance for the S protein, particularly in the context of controlling the S protein open-closed equilibrium, preventing S1 from premature shedding upon proteolytic cleavage, and higher order S protein complex formation. Consistently, mutations in the loop have been shown to reduce infectivity and expression of SARS-CoV-2, indicating a potential role for the loop in viral assembly (Bangaru et al., 2020). In our simulations, the MM pocket behind the 617-628 loop interacted with one, two, or rarely three benzene molecules at any given time (Figure 6A and S6B). A multiple sequence alignment indicates that the surface of the MM pocket is well-conserved across different coronaviruses (Figure S7A-B). Interestingly, the pocket also contains residue D614 which, when mutated to glycine, results in faster viral transmission, more efficient infection and replication (Hou et al., 2020), and higher S protein density on the viral surface (Zhang et al., 2020). The up-down dynamics of the RBD in D614G S protein correlates with order-disorder conformational changes of the 617-628 loop (Zhang et al., 2021), suggesting that targeting the nearby MM

pocket could affect the propensity for RBD opening. Moreover, destabilising hydrophobic interactions between this loop and CTD2 may promote S1 shedding and therefore reduce the stability of a cleaved S protein trimer. Additionally, the pocket is within close proximity to residue A570, which is mutated to aspartate in the SARS-CoV-2 Alpha (B.1.1.7) variant, as well as residue H655, which is mutated to tyrosine in the SARS-CoV-2 Gamma (P.1) and Omicron (B.1.1.529) variants; all three variants of concern are associated with increased transmissibility and immune evasion (Figure S7C) (Davies et al., 2020; Planas et al., 2021). Thus, the predominantly hydrophobic nature of the pocket, its potential to interact with aromatic moieties commonly present in the drug molecules, its well conserved surfaces and, most importantly, its proximity to the functionally relevant 617-628 loop and mutated residues in novel SARS-CoV-2 variants with higher transmission rate, are all promising indicators of the potential druggability of the MM pocket.

Our discovery of the MM pocket allows for future exploratory studies including virtual screening of small molecules that may bind to the pocket, coupled to subsequent determination of the effect of binding upon the overall dynamics of the S protein. Due to the strategic location of the pocket vis-à-vis the crucial 617-628 loop described above, we hypothesize that targeting the MM pocket would disrupt the network of hydrophobic interactions between the loop and the CTD2 domain. This could potentially shift the loop dynamics to favour a disordered state, which would destabilize the S1 and S2 contacts upon proteolytic cleavage resulting in premature S1 shedding. Such local structural perturbations would be particularly advantageous against currently circulating SARS-CoV-2 variants of concern including Omicron as they all carry the D614G mutation, which prevents premature dissociation of the S1 subunit (Zhang et al., 2021). Additionally, a recent cryo-EM study suggested that in low pH conditions, as found in intracellular compartments where SARS-CoV-2 is assembled, the region containing the 617-628 loop adopts a fully ordered state resulting in a “locked” conformation of the S protein that prevents premature transition into open and post-fusion conformations during viral assembly (Qu et al., 2021). Disrupting this locked conformation by targeting the MM pocket could therefore reduce the number of functional S proteins in a mature virion.

Although the PS and LA pockets were previously characterised in S protein cryo-EM structures, those provided only a static description of the pockets in their most stable fully ligand-bound state. In this study, we elaborated on pocket dynamic properties, especially with regards to pocket opening and closing motions, the effect of glycans, and the possible route of ligand entry. The LA pocket in particular is an ongoing target for rational drug design and therefore important to address in terms of its dynamic properties. Our observation of a prominent entry route for benzene when RBD is in the down conformation provides an interesting finding that might be relevant for other LA pocket-binding ligands as well.

Furthermore, the accessibility of the pocket when in an up-state suggests that ligands might enter the pocket even when the RBD is pointing upwards. This is an important point in terms of drug design as the up-state allows for greater conformational freedom and more flexible entry routes for the ligands. Comparatively, the down-state RBD and its entry site are less accessible and might pose a steric hindrance for effective binding, especially if a given ligand is bulky or branched. Therefore, the upwards-pointing RBD might be easier to target with a drug molecule, after which its presence could subsequently stabilise the closed conformation that represents a receptor-binding incompetent state of the S protein.

In summary, we have demonstrated the power of the benzene mapping technique to delineate cryptic hydrophobic pockets that are of interest for drug and monoclonal antibody development targeting the SARS-CoV-2 S glycoprotein. In addition to successfully reproducing two independently identified cryptic pockets, we also uncovered a novel and potentially druggable pocket on the S protein ECD surface. The pocket was present in systems emulating both immature and mature glycosylation states, suggesting its druggability may not be dependent upon the stage of virus maturation. Overall, the predominantly hydrophobic nature of the cryptic pocket, its well conserved surface, and proximity to regions of functional relevance in viral assembly and fitness are all promising indicators of its potential for therapeutic targeting. Complementing efforts in antibody-based therapy and vaccine development, rational design of small-molecule drugs targeting S protein pockets may provide an essential therapeutic practice for combatting the COVID-19 pandemic.

Acknowledgements

This work was supported by BII of A*STAR. PJB, JKM and FS acknowledge funding from grant FY21_CF_HTPO SEED_ID_BII_C211418001 funded by A*STAR. LZ thanks the A*STAR Graduate Academy (A*GA) for funding. Simulations were performed on resources of the National Supercomputing Centre, Singapore (https://www.nscc.sg), the A*STAR Computational Resource Centre (A*CRC), Iridis 5 supercomputer at the University of Southampton, ARCHER provided by the UK HECBioSim, and the supercomputer Fugaku provided by RIKEN through the HPCI System Research Project (Project ID: hp200303). GSA acknowledges Startup Funds from The Pennsylvania State University.

Authors contributions

Conceptualization, L.Z., F.S., P.J.B.; Methodology, L.Z., F.S., A.T.S., P.V.R.; Investigation, L.Z., F.S., A.T.S., P.V.R., J.K.M., A.B., C.P., N.K.T.; Formal Analysis, L.Z., F.S., P.V.R.; Visualization, L.Z., F.S., P.V.R; Writing – Original Draft, L.Z., F.S., P.V.R., P.J.B; Writing – Review & Editing, L.Z., F.S., P.V.R., J.W., P.M., M.C., S.K., G.S.A, P.J.B; Supervision, J.W.,

P.M., M.C., S.K., G.S.A, P.J.B; Project Administration, J.W., P.M., M.C., S.K., G.S.A, P.J.B.; Funding Acquisition, J.W., P.M., M.C., S.K., G.S.A, P.J.B.

Declaration of interests

The authors declare no competing interests.

Main figure titles and legends

Figure 1. S protein bending dynamics during simulations without benzene. (A) Full length model of the S glycoprotein with the protein shown in cartoon representation and coloured pink (chain A), cyan (chain B) and green (chain C), with the glycans and palmitoylated cysteine residues shown in stick representation and coloured yellow and brown, respectively. The different subdomains are labelled as RBD (receptor binding domain), NTD (N-terminal domain), HR1 (heptad repeat 1), CH (central helix), CD (connector domain), HR2 (heptad repeat 2), and TM (transmembrane domain). Enlarged image shows loop 620-640 in red nearby the NTD, CTD1 (C-terminal domain 1) and CTD2 (C-terminal domain 2), with nearby residues D614 and K854 shown in stick representation. **(B)** (Left) A snapshot from the end of a simulation of S protein open conformation with dominant glycans. The protein and glycans are coloured as in 1A, while the lipid phosphorus atoms are shown in sphere representation and coloured grey. (Right) Top, bending angle, Θ, measured as the acute angle between the centres of mass of the ECD (residue 27-1141), the hinge region (residue 1142-1156) and the HR2 domain (residue 1157-1207). Bottom, bending angle, Ψ, measured as the acute angle between the HR2 domain, the hinge region (residue 1208-1212) and the TM domain (residue 1213-1239). Black, dominant glycans; blue, mannose glycans; red, no glycans. (C) Snapshots of S protein at 10 ns intervals from a simulation, fitted onto the TM domain. The RBD is highlighted in surface representation. Glycan molecules are omitted for clarity. See also Figure S1, S2 and S3.

Figure 2. S protein shielding by glycans during simulations without benzene. (A) Snapshots of S protein ECD (top) and stalk (bottom) coloured cyan, pink and green with glycans in yellow at 10 ns intervals from a simulation of S protein with dominant glycans. **(B)** Solvent accessible surface area (SASA) of the ECD (top) and the stalk (bottom). Black, dominant glycans; blue, mannose glycans; red, no glycans. Percentage of surface area buried by glycans is shown on the right, average from the last 50 ns of the simulations with the error bars showing standard deviations along the trajectories. The radius of solvent probe used for calculation was 0.14 nm.

Figure 3. S protein cryptic pockets revealed during simulations in the presence of benzene. LA and PS pockets are named according to their bound ligands (shown in licorice representation in insets), as their binding sites have previously been identified by cryo-EM (Bangaru et al., 2020; Carrique et al., 2020; Toelzer et al., 2020). Multimerization (MM) pocket is a surface groove which extends down the interchain interface and underneath the 617-628 loop (labelled in inset). Pockets are shown as clusters of grey (apolar) and red (polar) spheres. The three chains of S protein are coloured as in Figure 1. See also Figure S4.

Figure 4. PS pocket properties and opening motions. (A) Apolar surface area of the PS pocket across different glycoforms and separated by solvent composition. The dashed line denotes the averaged pocket SASA for cryo-EM structures with bound ligands (PDB codes: 7JJI (Bangaru et al., 2020), 7NTA, and 7NT9 (Rosa et al., 2021)). *p*-value significance values were calculated using Wilcoxon signed-rank test (****: $p \leq 0.0001$; ***: $p \leq 0.001$; **: $p \leq 0.01$; *: $p \leq 0.05$; *ns* > 0.05). “Dominant glycans”, “mannose glycans”, and “no glycans” refers to systems in which the S protein has been modelled with either the most dominant glycan species (Watanabe et al., 2020), oligomannose-type glycans, or without glycans present, respectively. The boxed segment displays the average proportion of polar vs. apolar surface area of the PS pocket. **(B)** Ligands bound within the PS pocket. PS and biliverdin binding modes are determined from cryo-EM experiments (PDB codes 7JJI and 7NT9, respectively), while a simulation snapshot is used to display benzene molecules in the PS pocket. The NTD is shown in blue ribbons and transparent surface representation; Cα atoms of labelled residues are featured as yellow spheres; ligands are shown in licorice and coloured by atom types. **(C)** Distance measurements between the upper edge (residues 167-180) and lower edge (residues 187, 209-232) segments of the PS pocket. Distance distributions described in violin plots include pooled values from both control (- bnz) and benzene (+ bnz) simulations. **(D)** The span of motion that describes the opening of the PS pocket. Individual snapshots are distinguished by different-coloured Cα spheres. The wide conformations appear only in unglycosylated systems.

Figure 5. LA pocket properties and benzene binding patterns. (A) Apolar surface area of the LA pocket across different glycoforms, solvent compositions and RBD conformations (up vs. down state). The dashed line corresponds to the average apolar SASA for the cryo-EM structure in the presence of bound LA (PDB code: 7JJI (Bangaru et al., 2020)). Plot descriptors are the same as in Figure 4A. **(B)** Number of per-residue benzene contacts averaged over the course of the simulation. The most prominent contacts for the down-state are highlighted in grey on the plot and labelled on the corresponding structure. The RBD structure is shown in cartoon representation – 'up' in purple and ‘down’ in green. LA pocket residues are shown as

sticks and coloured based on the number of benzene contacts. The down conformation also contains benzene probes bound into the LA pocket, shown as orange spheres. The arrows denote likely routes of ligand entry: solvent-exposed up conformation displays multiple entry pathways, whereas down conformation consistently reveals a single pathway flanked by Tyr369, Ala372, and Phe374 residues. See also Figure S5.

Figure 6. Properties of the MM pocket. (A) S protein snapshot in surface representation with colour-coded chains and an inset image showing a portion of the MM pocket packed underneath the 617-628 loop. Three benzene molecules (in orange) interact with the protein surface and occupy a predominantly hydrophobic binding pocket (spheres representing the pocket are colour coded as in Figure 3). **(B)** Apolar surface areas of the MM pocket are shown as violin plots and labelled as in Figure 3. Similar to positive controls, the addition of benzene to the system increases overall apolar component of the pocket in question. **(C)** MM pocket shown in ribbon representation and coloured according to average number of per-residue glycan contacts (calculated across both high-mannose and dominant glycan systems). Glycans predominantly interacted with the 617-628 loop, whereas the pocket interior is not in contact with any glycan component. See also Figure S6 and S7.

Figure 7. The dynamic properties of the 617-632 peptide. HDX-MS mass spectrum of the peptide at labelled time points (left) shows a bimodal profile with a minor higher exchange population, indicating a conformational ensemble property in solution. In MD simulations, the loop containing this peptide exhibits a similar bimodal characteristic as assessed via solvent-accessible surface area (SASA) and conformational cluster analysis (right).

STAR METHODS

RESOURCE AVAILABILITY

Lead contact

Further information and requests for resources should be directed to and will be fulfilled by the Lead Contact, Peter J. Bond (peterjb@bii.a-star.edu.sg).

Materials availability

This study did not generate new materials.

Data and code availability

- SARS-CoV-2 models have been deposited at Zenodo and are publicly available as of the date of publication. DOIs are listed in the key resources table. HDX data have been deposited at ProteomeXchange Consortium and is publicly available as of the date of publication. The accession number is listed in the key resources table.
- This paper does not report original code.
- Any additional information required to reanalyse the data reported in this paper is available from the lead contact upon request.

EXPERIMENTAL MODEL AND SUBJECT DETAILS

SARS-CoV-2 S Glycoprotein models

A full-length model of the wild-type SARS-CoV-2 S protein was built using integrative modelling with a combination of cryo-EM and NMR structures as templates. Three glycoforms of the model were generated: i) with dominant glycans based on mass spectrometric data, ii) with oligomannose-type glycans, and iii) with no glycans. Further details are provided in Method Details section below.

METHODS DETAILS

Integrative Homology Modelling

The S protein RBD defines its predominant functional state, with the open state having one RBD in the “up” conformation, allowing for binding to the host ACE2 receptor (Shang et al., 2020; Yan et al., 2020), with the other two RBDs in the “down” conformation interacting with NTD and other subdomains. We first built a complete model of the SARS-CoV-2 S protein in this open “up-down-down” RBD configuration using Modeller version 9.21 (Sali and Blundell, 1994). The full sequence was obtained from the complete genome of SARS-CoV-2 (GenBank: MN908947) (Wu et al., 2020). The cryo-EM structure of the S protein ECD in the open state (PDB: 6VSB) (Wrapp et al., 2020) was used as the main template for the ECD. Missing loops in the RBD up state were modelled using the cryo-EM structure of SARS-CoV-2 RBD bound to the angiotensin converting enzyme (ACE) 2 receptor (PDB: 6M17) (Yan et al., 2020), while

missing loops in the N-terminal domain (NTD) and the C-terminus of the ECD were modelled using the cryo-EM structure of S ECD in the closed state resolved at a higher resolution (PDB: 6XR8) (Cai et al., 2020). The heptad repeat 2 (HR2) domain was modelled based on the NMR structure of SARS-CoV HR2 domain (96% sequence identity) in the prefusion conformation (PDB: 2FXP) (Hakansson-McReynolds et al., 2006). To date, there is no structural information for the transmembrane (TM) domain of the S protein from any coronaviruses. To estimate the position of the TM domain, the PSIPRED secondary structure prediction web server was used (Jones, 1999). The server predicted residue 1213-1237 to be within the TM helix. The presence of a GxxxG motif within this sequence suggests that the three helices of the S protein subunits form an oligomeric assembly in the membrane (Teese and Langosch, 2015). We therefore used the putative TM domain sequence to search for a homotrimeric TM structure with reasonable sequence similarity. The NMR structure of human immunodeficiency virus 1 (HIV-1) gp-41 TM domain (PDB: 5JYN) (Dev et al., 2016), which shares 27% sequence identity, was subsequently used as template. Ten models were built and the three models with the lowest discreet optimised protein energy (DOPE) scores (Shen et al., 2006) were chosen for further stereochemical assessment using Ramachandran analysis (Ramachandran et al., 1963). The model with the lowest number of outlier residues was subsequently selected for further modifications.

Two post-translational modifications were incorporated into the models: palmitoylation and glycosylation. Palmitoylation of two cysteine clusters in the SARS-CoV S protein has been shown to be important in membrane fusion with the host cell (Petit et al., 2007). We therefore added palmitoylation to cysteine residues at position 1236, 1240 and 1243 found in these two membrane proximal clusters. There are 22 N-glycosylation sites on each subunit of the S proteins, which likely play a crucial role in immune evasion by blocking access to protein epitopes. For each model, we built three glycoforms: i) with the most dominant glycan found on each site based on mass spectrometric data (Watanabe et al., 2020); ii) with an oligomannose-type glycan ($Man_9GlcNAc_2$) on all sites to represent the unprocessed glycosylated protein; and iii) without glycans. Palmitoylation and glycosylation of the S protein models was performed using the CHARMM-GUI Glycan Reader and Modeller web server (Park et al., 2019).

(Klumperman et al., 1994; Krijnse-Locker et al., 1994)(Klumperman et al., 1994; Krijnse-Locker et al., 1994)(Klumperman et al., 1994; Krijnse-Locker et al., 1994)(Klumperman et al., 1994; Krijnse-Locker et al., 1994)(Klumperman et al., 1994; Krijnse-Locker et al., 1994)To simulate the S protein in its native membrane environment (Klumperman et al., 1994; Krijnse-Locker et al., 1994), we embedded our models in an endoplasmic reticulum-Golgi intermediate compartment (ERGIC) membrane. A 25 x 25 nm^2 patch representing the ERGIC membrane was built using the CHARMM-GUI Membrane Builder web server (Lee et al., 2019).

The membrane is symmetric and the composition is 47% phosphatidylcholine (PC), 20% phosphatidylethanol amine (PE), 11% phosphatidylinositol phosphate (PIP), 7% phosphatidylserine (PS) and 15% cholesterol (Casares et al., 2019; Meer, 1998; van Meer et al., 2008).

Molecular Dynamics Simulations of Benzene-free Systems

The CHARMM36 force field was used to parametrize the full-length S glycoprotein models (Huang and MacKerell, 2013). The protein was inserted into the model membrane based on the position of the TM domain. Overlapping lipid residues were removed and the steepest descent method was performed to minimize the system. The system was solvated with TIP3P water molecules and neutralised with 0.15 M NaCl salt. Step-wise minimization and equilibration adapted from CHARMM-GUI standard protocols were performed (Lee et al., 2016). During equilibration, the temperature of the system was maintained at 310 K using the Berendsen thermostat with a time constant of 1 ps, while the pressure was kept at 1 atm by a semi-isotropic pressure coupling using the Berendsen barostat with a time constant of 5 ps (Berendsen et al., 1984). The smooth particle mesh Ewald (PME) method (Essmann et al., 1995) with a real-space cut-off of 1.2 nm was utilised to calculate the electrostatic interactions, whereas the Van der Waals interactions were truncated at 1.2 nm and the force switch smoothing function applied between 1.0 to 1.2 nm. An integration time step of 1 fs and 2 fs were used at the early and late steps of equilibration, respectively, with the LINCS algorithm utilised to constrain all covalent bonds with hydrogen atoms (Hess et al., 1997). After equilibration, 200 ns production simulations were conducted. The Nosé-Hoover thermostat with a time constant of 1 ps was used to maintain the temperature (Hoover, 1985; Nosé, 1984), while the Parrinello-Rahman barostat with a time constant of 5 ps was used to maintain the pressure (Parrinello, 1981). A 2-fs integration time step was employed during this run.

Molecular Dynamics Simulations of Benzene Systems

A protocol for setting up benzene probe simulations in membrane systems was adapted from our previous work (Zuzic et al., 2020). Benzene molecule partial charges were adjusted from phenylalanine aromatic ring parameters defined in CHARMM36 force field (Huang and MacKerell, 2013) so that the distribution of charges was uniform across all six carbon atoms. A virtual site was added at a geometric centre of each benzene molecule, and it served as a point of repulsion between the benzene probe and the membrane. As the membrane composition differed from the one used in the original paper, repulsion point positions and the Lennard-Jones σ-value had to be adjusted to be effective for the ERGIC membrane composition. A repulsion point was placed on a carboxyl oxygen (O22/O32), one in each fatty acid tail. Repulsion point atoms were present in all lipid types (including protein-bound

palmitoyl group), except for cholesterol. To account for increased gaps between membrane repulsion points due to the presence of cholesterol, the σ-value for the interactions between benzene dummy atoms and membrane repulsion points was increased to 1.4 nm. The setup was tested for the effects of aggregation and probe sequestration on a small ERGIC membrane (7 nm × 7 nm) and during a 100 ns simulation, benzene molecules remained solvated and outside the bilayer.

Benzene probes were added to a simulation box in a 0.2 M concentration. A lower probe concentration allowed for the omission of benzene-benzene repulsions and exclusions, as the probes were less likely to aggregate (Tan et al., 2016). Subsequently, the rest of the system was solvated with TIP3P water and 0.15 M NaCl salt. Minimization, equilibration, and production simulations followed the same protocol as for the benzene-free systems. To determine if the structural distortion caused by benzene on the HR2 domain in full length S protein simulations has any impact on the formation of cryptic pockets, we repeated our dominant glycans S protein benzene simulations using only the ECD (residue 14-1146). For these simulations, the backbone of the last five residues on the C-terminus was positionally restrained with a force constant of 1000 kJ mol^{-1} nm^{-2}. All simulations were performed with GROMACS 2018 (Abraham et al., 2015) and the list of simulations is provided in Table S1.

Hydrogen-Deuterium Exchange Mass Spectrometry

Deuterium exchange mass spectra of the peptide 617-632 is reported from the data deposited in PreoteomeXchange Consotium via the PRIDE partner repository (Vizca et al., 2016) with dataset identifier: PXD23138 and reported by Palur et al. (Raghuvamsi et al., 2021). Briefly, Deuterium exchange reaction was performed by incubating purified recombinant S protein (PBS, pH 7.4) in PBS buffer containing 90% D_2O at 37°C for 1, 10 and 100 minute of labelling time. The deuterium exchange reaction was stopped by mixing the reaction mixture with prechilled quenched buffer (1.5 M GnHCl and 0.25 M Tris(2-carboxyethyl) phosphine-hydrochloride (TCEP-HCl)) to lower the pH to 2.4 and incubated in ice for 1 minute before online pepsin digestion and mass spectrometry analysis. Quenched samples were injected into nanoUPLC HDX sample manager (Waters, Milford, MA). Immobilised Waters Emzymate BEH pepsin column (2.1 × 30 mm) was used to perform online digestion in 0.1% formic acid in water at 100 µl min^{-1} flow rate. Pepsin-proteolysed peptides were trapped in a 2.1 × 5 mm C18 trap (ACQUITY BEH C18 VanGuard Pre-column, 1.7 µm, Waters, Milford, MA). Elution of trapped peptides was performed using acetonitrile gradient of 8% to 40% in 0.1% formic acid at flow rate 40 µl min^{-1} into reverse phase column (ACQUITY UPLC BEH C18 Column, 1.0 × 100 mm, 1.7 µm, Waters) pumped by nanoACQUITY Binary Solvent Manager (Waters, Milford, MA). Electrospray ionisation mode was used to spray ionised peptides and HDMSE mode of detection was implemented on SYNAPT G2-Si mass spectrometer (Waters, Milford,

MA). 200 fmol μl^{-1} of [Glu1]-fibrinopeptide B ([Glu1]-Fib) is injected for lock spray correction at a flow rate of 5 $\mu l\ min^{-1}$. Protein Lynx Global Server (PLGS v3.0, HDMSE mode) was used to identify the mass spectra of undeuterated protein samples on a separate sequence database of each protein sequence. Further, peptides were filtered using minimum intensity cutoffs of 2500 for product and precursor ions, precursor ion mass tolerance of <10 ppm and minimum products per amino acids of 0.2 using DynamX v 3.0 (Waters, Milford, MA). All the experiments were performed in triplicate and not corrected for back exchange.

Analysis

Protein, sugar and membrane structural properties were analysed using GROMACS tools, MDAnalysis (Michaud-agrawal et al., 2011) and VMD (Humphrey and Dalke, 1996). Pockets on the surface of the S protein ectodomain were analysed using MDPocket (Schmidtke et al., 2011). Initial pocket mapping of the entire ectodomain structure was followed by repeated mapping and property characterisation of each individual pocket of interest. Pockets were analysed across all simulated trajectories in 5 ns snapshot intervals. Pocket SASA was determined by calculating apolar contribution of all surrounding residues using GROMACS analysis tools. Benzene and glycan contact maps in pockets were calculated in VMD (Humphrey et al., 1996). Sequence conservation of the S protein was analysed using the ConSurf webserver (Ashkenazy et al., 2016). The HMMER algorithm (Eddy, 1998) was used to pull 40 unique sequences with 35-95% sequence identity to the SARS-CoV-2 S protein (GenBank: MN908947) (Wu et al., 2020) from the UniProt database (Consortium, 2019). Multiple sequence alignment was built using the MAFFT program (Rozewicki et al., 2019). Structures were visualised using VMD (Humphrey et al., 1996) and USCF ChimeraX (Pettersen et al., 2021).

QUANTIFICATION AND STATISTICAL ANALYSIS

No statistical analysis was performed.

ADDITIONAL RESOURCES

No additional resources were used.

References

Abraham, M.J., Murtola, T., Schulz, R., Páll, S., Smith, J.C., Hess, B., and Lindahl, E. (2015). GROMACS: High performance molecular simulations through multi-level parallelism from laptops to supercomputers. SoftwareX *1*, 19–25.

Ashkenazy, H., Abadi, S., Martz, E., Chay, O., Mayrose, I., Pupko, T., and Ben-Tal, N. (2016). ConSurf 2016: an improved methodology to estimate and visualize evolutionary conservation in macromolecules. Nucleic Acids Res. *44*, W344–W350.

Bangaru, S., Ozorowski, G., Turner, H.L., Antanasijevic, A., Huang, D., Wang, X., Torres, J.L., Diedrich, J.K., Tian, J.-H., Portnoff, A.D., et al. (2020). Structural analysis of full-length SARS-CoV-2 spike protein from an advanced vaccine candidate. Science (80-.). *370*, 1089–1094.

Berendsen, H.J.C., Postma, J.P.M., van Gunsteren, W.F., DiNola, A., and Haak, J.R. (1984). Molecular dynamics with coupling to an external bath. J. Chem. Phys. *81*, 3684.

Cai, Y., Zhang, J., Xiao, T., Peng, H., Sterling, S.M., Walsh, R.M., Rawson, S., Rits-Volloch, S., and Chen, B. (2020). Distinct conformational states of SARS-CoV-2 spike protein. Science (80-.). *21*, 1586–1592.

Carrique, L., Duyvesteyn, H.M., Malinauskas, T., Zhao, Y., Ren, J., Zhou, D., Walter, T.S., Radecke, J., Huo, J., Ruza, R.R., et al. (2020). The SARS-CoV-2 Spike harbours a lipid binding pocket which modulates stability of the prefusion trimer. BioRxiv 1–29.

Casalino, L., Gaieb, Z., Goldsmith, J.A., Hjorth, C.K., Dommer, A.C., Harbison, A.M., Fogarty, C.A., Barros, E.P., Taylor, B.C., Mclellan, J.S., et al. (2020). Beyond Shielding: The Roles of Glycans in the SARS-CoV-2 Spike Protein. ACS Cent. Sci. *6*, 1722–1734.

Casares, D., Escribá, P. V., and Rosselló, C.A. (2019). Membrane lipid composition: Effect on membrane and organelle structure, function and compartmentalization and therapeutic avenues. Int. J. Mol. Sci. *20*, 1–30.

Chiliveri, S.C., Louis, J.M., Ghirlando, R., and Bax, A. (2021). Transient lipid-bound states of spike protein heptad repeats provide insights into SARS-CoV-2 membrane fusion. Sci. Adv. *7*, 1–13.

Choi, Y.K., Cao, Y., Frank, M., Woo, H., Park, S.J., Yeom, M.S., Croll, T.I., Seok, C., and Im, W. (2021). Structure, Dynamics, Receptor Binding, and Antibody Binding of the Fully Glycosylated Full-Length SARS-CoV-2 Spike Protein in a Viral Membrane. J. Chem. Theory Comput. *17*, 2479–2487.

Consortium, T.U. (2019). UniProt: A worldwide hub of protein knowledge. Nucleic Acids Res. *47*, D506–D515.

Costello, S.M., Shoemaker, S.R., Hobbs, H.T., Nguyen, A.W., Hsieh, C.-L., Maynard, J.A., McLellan, J.S., Pak, J.E., and Marqusee, S. (2022). The SARS-CoV-2 spike reversibly samples an open-trimer conformation exposing novel epitopes. Nat. Struct. Mol. Biol. *29*.

Davies, N.G., Barnard, R.C., Jarvis, C.I., Kucharski, A.J., Munday, J., Pearson, C.A.B., Russell, T.W., Tully, D.C., Abbott, S., Gimma, A., et al. (2020). Estimated transmissibility and severity of novel SARS-CoV-2 Variant of Concern 202012/01 in England. MedRxiv.

Dev, J., Park, D., Fu, Q., Chen, J., Ha, H.J., Ghantous, F., Herrmann, T., Chang, W., Liu, Z., Frey, G., et al. (2016). Structural basis for membrane anchoring of HIV-1 envelope spike. Science (80-.). *353*, 172–175.

Eddy, S.R. (1998). Profile hidden Markov models. Bioinformatics *14*, 755–763.

Ellis, D., Brunette, N., Crawford, K.H.D., Walls, A.C., Pham, M.N., Chen, C., Herpoldt, K.-L., Fiala, B., Murphy, M., Pettie, D., et al. (2021). Stabilization of the SARS-CoV-2 Spike Receptor-Binding Domain Using Deep Mutational Scanning and Structure-Based Design. Front. Immunol. *12*, 1–17.

Englander, S.W., Sosnick, T.R., Englander, J.J., and Mayne, L. (1996). Mechanisms and uses of hydrogen exchange. Curr. Opin. Struct. Biol. *6*, 18–23.

Essmann, U., Perera, L., Berkowitz, M.L., Darden, T., Lee, H., and Pedersen, L.G. (1995). A smooth particle mesh Ewald method. J. Chem. Phys. *103*, 8577.

Gorbalenya, A.E., Baker, S.C., Baric, R.S., de Groot, R.J., Drosten, C., Gulyaeva, A.A., Haagmans, B.L., Lauber, C., Leontovich, A.M., Neuman, B.W., et al. (2020). The species Severe acute respiratory syndrome-related coronavirus: classifying 2019-nCoV and naming

it SARS-CoV-2. Nat. Microbiol. *5*, 536–544.
Hakansson-McReynolds, S., Jiang, S., Rong, L., and Caffrey, M. (2006). Solution structure of the severe acute respiratory syndrome-coronavirus heptad repeat 2 domain in the prefusion state. J. Biol. Chem. *281*, 11965–11971.
Hess, B., Bekker, H., Berendsen, H.J.C., and Fraaije, J.G.E.M. (1997). LINCS: A linear constraint solver for molecular simulations. J. Comp. Chem. *18*, 1463–1472.
Hoover, W.G. (1985). Canonical dynamics: Equilibrium phase-space distributions. Phys. Rev. A *31*, 1695–1697.
Hou, Y.J., Chiba, S., Halfmann, P., Ehre, C., Kuroda, M., Dinnon, K.H., Leist, S.R., Schäfer, A., Nakajima, N., Takahashi, K., et al. (2020). SARS-CoV-2 D614G variant exhibits efficient replication ex vivo and transmission in vivo. Science (80-.). *370*, 1464–1468.
Huang, J., and MacKerell, A.D. (2013). CHARMM36 all-atom additive protein force field: Validation based on comparison to NMR data. J. Comput. Chem. *34*, 2135–2145.
Humphrey, W., and Dalke, A. (1996). VMD: visual molecular dynamics. J. Mol. Graph. *15*, 33–38.
Humphrey, W., Dalke, A., and Schulten, K. (1996). VMD: Visual Molecular Dynamics. J. Mol. Graph. *14*, 33–38.
Jones, D.T. (1999). Protein secondary structure prediction based on position-specific scoring matrices. J. Mol. Biol. *292*, 195–202.
Ke, Z., Oton, J., Qu, K., Cortese, M., Zila, V., McKeane, L., Nakane, T., Zivanov, J., Neufeldt, C.J., Lu, J.M., et al. (2020). Structures, conformations and distributions of SARS-CoV-2 spike protein trimers on intact virions. Nature *588*, 498–502.
Klumperman, J., Locker, J.K., Meijer, A., Horzinek, M.C., Geuze, H.J., and Rottier, P.J. (1994). Coronavirus M proteins accumulate in the Golgi complex beyond the site of virion budding. J. Virol. *68*, 6523–6534.
Korber, B., Fischer, W.M., Gnanakaran, S., Yoon, H., Theiler, J., Abfalterer, W., Hengartner, N., Giorgi, E.E., Bhattacharya, T., Foley, B., et al. (2020). Tracking Changes in SARS-CoV-2 Spike: Evidence that D614G Increases Infectivity of the COVID-19 Virus. Cell *182*, 812-827.e19.
Krijnse-Locker, J., Ericsson, M., Rottier, P.J.M., and Griffiths, G. (1994). Characterization of the budding compartment of mouse hepatitis virus: Evidence that transport from the RER to the Golgi complex requires only one vesicular transport step. J. Cell Biol. *124*, 55–70.
Kuzmanic, A., Bowman, G.R., Juarez-Jimenez, J., Michel, J., and Gervasio, F.L. (2020). Investigating Cryptic Binding Sites by Molecular Dynamics Simulations. ACS Appl. Mater. Interfaces *53*, 654–661.
Lan, J., Ge, J., Yu, J., Shan, S., Zhou, H., Fan, S., Zhang, Q., Shi, X., Wang, Q., Zhang, L., et al. (2020). Structure of the SARS-CoV-2 spike receptor-binding domain bound to the ACE2 receptor. Nature *581*, 215–220.
Lee, J., Cheng, X., Swails, J.M., Yeom, M.S., Eastman, P.K., Lemkul, J.A., Wei, S., Buckner, J., Jeong, J.C., Qi, Y., et al. (2016). CHARMM-GUI Input Generator for NAMD, GROMACS, AMBER, OpenMM, and CHARMM/OpenMM Simulations Using the CHARMM36 Additive Force Field. J. Chem. Theory Comput. *12*, 405–413.
Lee, J., Patel, D.S., Ståhle, J., Park, S.J., Kern, N.R., Kim, S., Lee, J., Cheng, X., Valvano, M.A., Holst, O., et al. (2019). CHARMM-GUI Membrane Builder for Complex Biological Membrane Simulations with Glycolipids and Lipoglycans. J. Chem. Theory Comput. *15*, 775–786.
Ma, J., Su, D., Sun, Y., Huang, X., Liang, Y., Fang, L., Ma, Y., Li, W., Liang, P., and Zheng, S. (2021). Cryo-electron Microscopy Structure of S-Trimer, a Subunit Vaccine Candidate for COVID-19. J. Virol. *95*.
Meer, G. Van (1998). Lipids of the Golgi membrane. Trends Cell Biol. *8924*, 29–33.
van Meer, G., Voelker, D.R., Feigenson, G.W., and Meer, G. V (2008). Membrane lipids: where they are and how they behave. Nat. Rev. Mol. Cell Biol. *9*, 112–124.
Michaud-agrawal, N., Denning, E.J., Woolf, T.B., and Beckstein, O. (2011). Software News and Updates MDAnalysis : A Toolkit for the Analysis of Molecular Dynamics Simulations. J. Comput. Chem. *32*, 2319–2327.

Narang, D., Lento, C., and Wilson, D.J. (2020). HDX-MS: An analytical tool to capture protein motion in action. Biomedicines *8*, 1–20.
Nosé, S. (1984). A molecular dynamics method for simulations in the canonical ensemble. Mol. Phys. *52*, 255–268.
Oliveira, A.S.F., Shoemark, D.K., Ibarra, A., and Davidson, D. (2021). The fatty acid site is coupled to functional motifs in the SARS-CoV-2 spike protein and modulates spike allosteric behaviour. BioRxiv 1–18.
Park, S.J., Lee, J., Qi, Y., Kern, N.R., Lee, H.S., Jo, S., Joung, I., Joo, K., Lee, J., and Im, W. (2019). CHARMM-GUI Glycan Modeler for modeling and simulation of carbohydrates and glycoconjugates. Glycobiology *29*, 320–331.
Parrinello, M. (1981). Polymorphic transitions in single crystals: A new molecular dynamics method. J. Appl. Phys. *52*, 7182.
Petit, C.M., Chouljenko, V.N., Iyer, A., Colgrove, R., Farzan, M., Knipe, D.M., and Kousoulas, K.G. (2007). Palmitoylation of the cysteine-rich endodomain of the SARS-coronavirus spike glycoprotein is important for spike-mediated cell fusion. Virology *360*, 264–274.
Petruk, G., Puthia, M., Petrlova, J., Samsudin, F., Strömdahl, A.-C., Cerps, S., Uller, L., Kjellström, S., Bond, P.J., and Schmidtchen, A. (2021). SARS-CoV-2 Spike protein binds to bacterial lipopolysaccharide and boosts proinflammatory activity. J. Mol. Cell Biol. *12*, 916–932.
Pettersen, E.F., Goddard, T.D., Huang, C.C., Meng, E.C., Couch, G.S., Croll, T.I., Morris, J.H., and Ferrin, T.E. (2021). UCSF ChimeraX: Structure visualization for researchers, educators, and developers. Protein Sci. *30*, 70–82.
Planas, D., Saunders, N., Maes, P., Guivel-Benhassine, F., Planchais, C., Buchrieser, J., Bolland, W.H., Porrot, F., Staropoli, I., Lemoine, F., et al. (2021). Considerable escape of SARS-CoV-2 Omicron to antibody neutralization. Nature.
Qu, K., Xiong, X., Ciazynska, K.A., Carter, A.P., and Brigss, J.A. (2021). Structures and function of locked conformations of SARS-CoV-2 spike Kun. BioRxiv 1–23.
Raghuvamsi, P., Tulsian, N., Samsudin, F., Qian, X., Purushotorman, K., Yue, G., Kozma, M., Lescar, J., MacAry, P., and Anand, G. (2021). SARS-CoV-2 S protein ACE2 interaction reveals novel allosteric targets 2 3 Running Title: Spike-ACE2 interactions allosterically prime proteolytic processing of Spike. Elife 10:e63646.
Ramachandran, G.N., Ramakrishnan, C., and Sasisekharan, V. (1963). Stereochemistry of polypeptide chain configurations. J. Mol. Biol. *7*, 95–99.
Rosa, A., Pye, V.E., Graham, C., Muir, L., Seow, J., Ng, K.W., Cook, N.J., Rees-Spear, C., Parker, E., Silva dos Santos, M., et al. (2021a). SARS-CoV-2 recruits a haem metabolite to evade antibody immunity. Sci. Adv. *5*, 17.
Rosa, A., Pye, V.E., Graham, C., Muir, L., Seow, J., Ng, K.W., Cook, N.J., Rees-Spear, C., Parker, E., Silva dos Santos, M., et al. (2021b). SARS-CoV-2 recruits a haem metabolite to evade antibody immunity. Sci. Adv. abg7607.
Rozewicki, J., Li, S., Amada, K.M., Standley, D.M., and Katoh, K. (2019). MAFFT-DASH: Integrated protein sequence and structural alignment. Nucleic Acids Res. *47*, W5–W10.
Sali, A., and Blundell, T. (1994). Comparative protein modelling by satisfaction of spatial restraints. J. Mol. Biol. *234*, 779–815.
Sayyed-Ahmad, A., and Gorfe, A.A. (2017). Mixed-Probe Simulation and Probe-Derived Surface Topography Map Analysis for Ligand Binding Site Identification. J. Chem. Theory Comput. *13*, 1851–1861.
Schmidtke, P., Bidon-chanal, A., Luque, F.J., and Barril, X. (2011). MDpocket: Open-source cavity detection and characterization on molecular dynamics trajectories. Bioinformatics *27*, 3276–3285.
Shang, J., Ye, G., Shi, K., Wan, Y., Luo, C., Aihara, H., Geng, Q., Auerbach, A., and Li, F. (2020). Structural basis of receptor recognition by SARS-CoV-2. Nature *581*, 221–224.
Shen, M., Devos, D., Melo, F., and Sali, A. (2006). A composite score for predicting errors in protein structure models. Protein Sci. *15*, 1653–1666.
Shoemark, D.K., Colenso, C.K., Toelzer, C., Gupta, K., Sessions, R.B., Davidson, A.D.,

Berger, I., Schaffitzel, C., Spencer, J., and Mulholland, A.J. (2021). Molecular Simulations suggest Vitamins, Retinoids and Steroids as Ligands of the Free Fatty Acid Pocket of the SARS-CoV-2 Spike Protein**. Angew. Chemie *133*, 7174–7186.
Sikora, M., Gecht, M., Covino, R., and Hummer, G. (2020). Map of SARS-CoV-2 spike epitopes not shielded by glycans. BioRxiv.
Tan, Y.S., and Verma, C.S. (2020). Straightforward Incorporation of Multiple Ligand Types into Molecular Dynamics Simulations for Efficient Binding Site Detection and Characterization. J. Chem. Theory Comput. *16*, 6633–6644.
Tan, Y.S., Reeks, J., Brown, C.J., Thean, D., Ferrer Gago, F.J., Yuen, T.Y., Goh, E.T.L., Lee, X.E.C., Jennings, C.E., Joseph, T.L., et al. (2016). Benzene Probes in Molecular Dynamics Simulations Reveal Novel Binding Sites for Ligand Design. J. Phys. Chem. Lett. *7*, 3452–3457.
Tan, Z.W., Tee, W.-V., Samsudin, F., Guarnera, E., Bond, P.J., and Berezovsky, I.N. (2022). Allosteric perspective on the mutability and druggability of the SARS-CoV-2 Spike protein. Structure *30*, 2021.08.01.454696.
Teese, M.G., and Langosch, D. (2015). Role of GxxxG Motifs in Transmembrane Domain Interactions. Biochemistry *54*, 5125–5135.
Toelzer, C., Gupta, K., Yadav, S.K.N., Borucu, U., Davidson, A.D., Kavanagh Williamson, M., Shoemark, D.K., Garzoni, F., Staufer, O., Milligan, R., et al. (2020). Free fatty acid binding pocket in the locked structure of SARS-CoV-2 spike protein. Science (80-.). *370*, 725–730.
Turoňová, B., Sikora, M., Schürmann, C., Hagen, W.J.H., Welsch, S., Blanc, F.E.C., von Bülow, S., Gecht, M., Bagola, K., Hörner, C., et al. (2020). In situ structural analysis of SARS-CoV-2 spike reveals flexibility mediated by three hinges. Science (80-.). *370*, 203–208.
Vizca, J.A., Csordas, A., Griss, J., Lavidas, I., Mayer, G., Perez-riverol, Y., Reisinger, F., Ternent, T., Xu, Q., Wang, R., et al. (2016). Erratum: 2016 update of the PRIDE database and its related tools (Nucleic Acids Research (2016) 44:D1 (D447-D456) DOI: 10.1093/nar/gkv1145). Nucleic Acids Res. *44*, 11033.
Walls, A.C., Park, Y.-J., Tortorici, M.A., Wall, A., McGuire, A.T., and Veesler, D. (2020). Structure, Function, and Antigenicity of the SARS-CoV-2 Spike Glycoprotein. Cell 281–292.
Watanabe, Y., Allen, J.D., Wrapp, D., McLellan, J.S., and Crispin, M. (2020). Site-specific glycan analysis of the SARS-CoV-2 spike. Science (80-.). *369*, 330–333.
Wrapp, D., Wang, N., Corbett, K.S., Goldsmith, J.A., Hsieh, C.-L., Abiona, O., Graham, B.S., and McLellan, J.S. (2020). Cryo-EM structure of the 2019-nCoV spike in the prefusion conformation. Science (80-.). 1260–1263.
Wrobel, A., Benton, D.J., Xu, P., Roustan, C., Martin, S.R., Rosenthal, P.B., Skehel, J.J., and Gamblin, S.J. (2020). SARS-CoV-2 and bat RaTG13 spike glycoprotein structures inform on virus evolution and furin-cleavage effects. Nat. Struct. Mol. Biol. *27*, 763–767.
Wu, F., Zhao, S., Yu, B., Chen, Y.-M., Wang, W., Song, Z.-G., Hu, Y., Tao, Z.-W., Tian, J.-H., Pei, Y.-Y., et al. (2020). A new coronavirus associated with human respiratory disease in China. Nature *265–269*.
Xiong, X., Qu, K., Ciazynska, K.A., Hosmillo, M., Carter, A.P., Ebrahimi, S., Ke, Z., Scheres, S.H.W., Bergamaschi, L., Grice, G.L., et al. (2020). A thermostable, closed SARS-CoV-2 spike protein trimer. Nat. Struct. Mol. Biol. *27*, 934–941.
Yan, R., Zhang, Y., Li, Y., Xia, L., Guo, Y., and Zhou, Q. (2020). Structural basis for the recognition of the SARS-CoV-2 by full-length human ACE2. Science (80-.). 1444–1448.
Yao, H., Song, Y., Chen, Y., Wu, N., Xu, J., Sun, C., Zhang, J., Weng, T., Zhang, Z., Wu, Z., et al. (2020). Molecular Architecture of the SARS-CoV-2 Virus. Cell *183*, 730-738.e13.
Yurkovetskiy, L., Wang, X., Pascal, K.E., Tomkins-Tinch, C., Nyalile, T.P., Wang, Y., Baum, A., Diehl, W.E., Dauphin, A., Carbone, C., et al. (2020). Structural and Functional Analysis of the D614G SARS-CoV-2 Spike Protein Variant. Cell *183*, 739-751.e8.
Zhang, J., Cai, Y., Xiao, T., Lu, J., Peng, H., Sterling, S.M., Walsh, R.M., Rits-Volloch, S., Zhu, H., Woosley, A.N., et al. (2021). Structural impact on SARS-CoV-2 spike protein by D614G substitution. Science (80-.). *372*, 525–530.

Zhang, L., Jackson, C.B., Mou, H., Ojha, A., Peng, H., Quinlan, B.D., Rangarajan, E.S., Pan, A., Vanderheiden, A., Suthar, M.S., et al. (2020). SARS-CoV-2 spike-protein D614G mutation increases virion spike density and infectivity. Nat. Commun. *11*, 6013.
Zimmerman, M., Porter, J., Ward, M., Singh, S., Vithani, N., Meller, A., Mallimadugula, U., Kuhn, C., Borowsky, J., Wiewiora, R., et al. (2021). SARS-CoV-2 Simulations Go Exascale to Capture Spike Opening and Reveal Cryptic Pockets Across the Proteome. Nat. Chem.
Zuzic, L., Marzinek, J.K., Warwicker, J., and Bond, P.J. (2020). A Benzene-Mapping Approach for Uncovering Cryptic Pockets in Membrane-Bound Proteins. J. Chem. Theory Comput. 5948–5959.

Figure 1

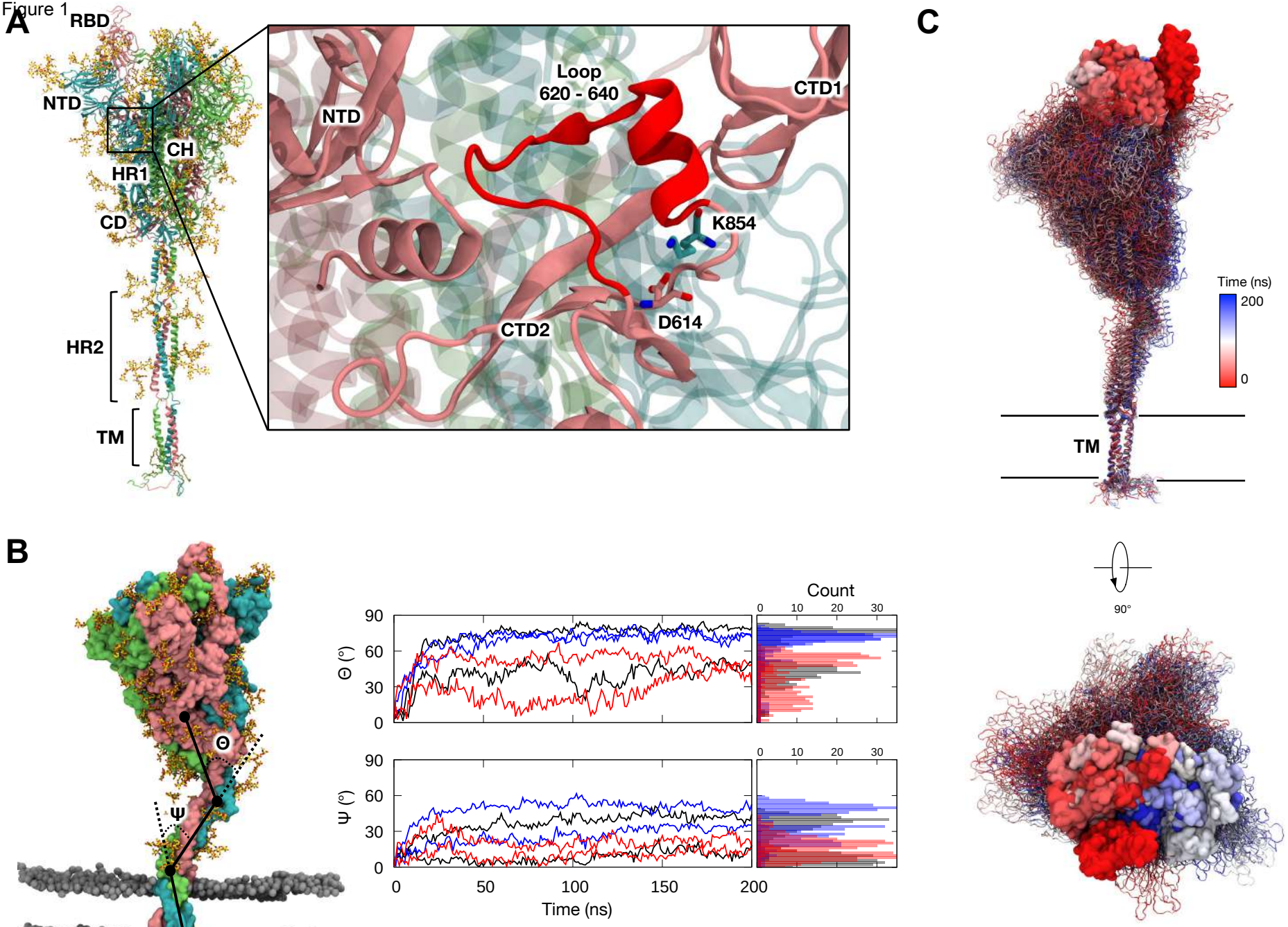
A
RBD
NTD
CH
HR1
CD
HR2
TM
Loop
620 - 640
CTD1
K854
D614
CTD2
B
Θ
Ψ
Count
0
10
20
30
90
60
30
0
Θ (°)
Ψ (°)
0
50
100
150
200
Time (ns)
C
Time (ns)
200
0
TM
90°

Figure 2

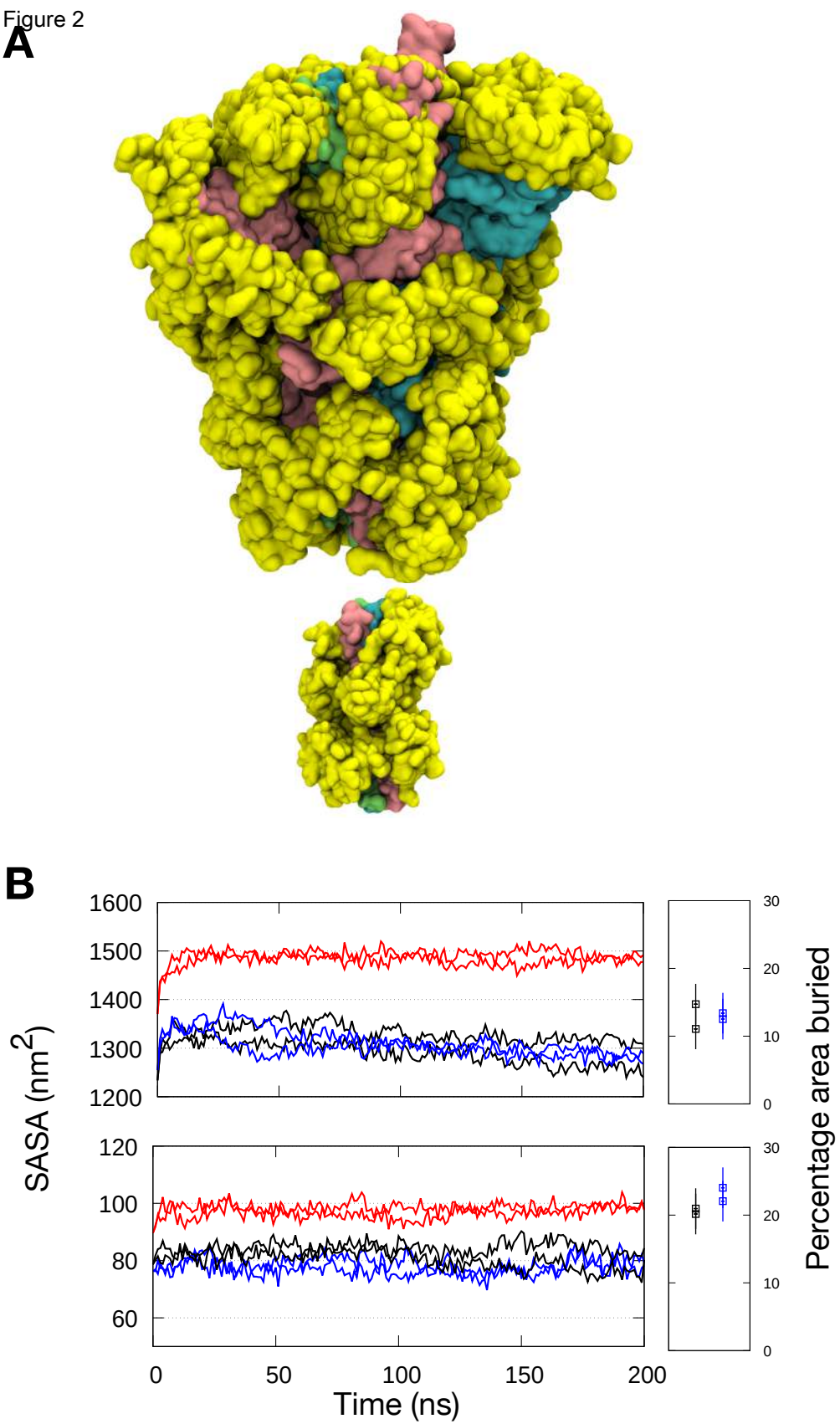
A
B
SASA (nm2)
Percentage area buried
Time (ns)
1600
1500
1400
1300
1200
120
100
80
60
30
20
10
0
0
50
100
150
200

Figure 3

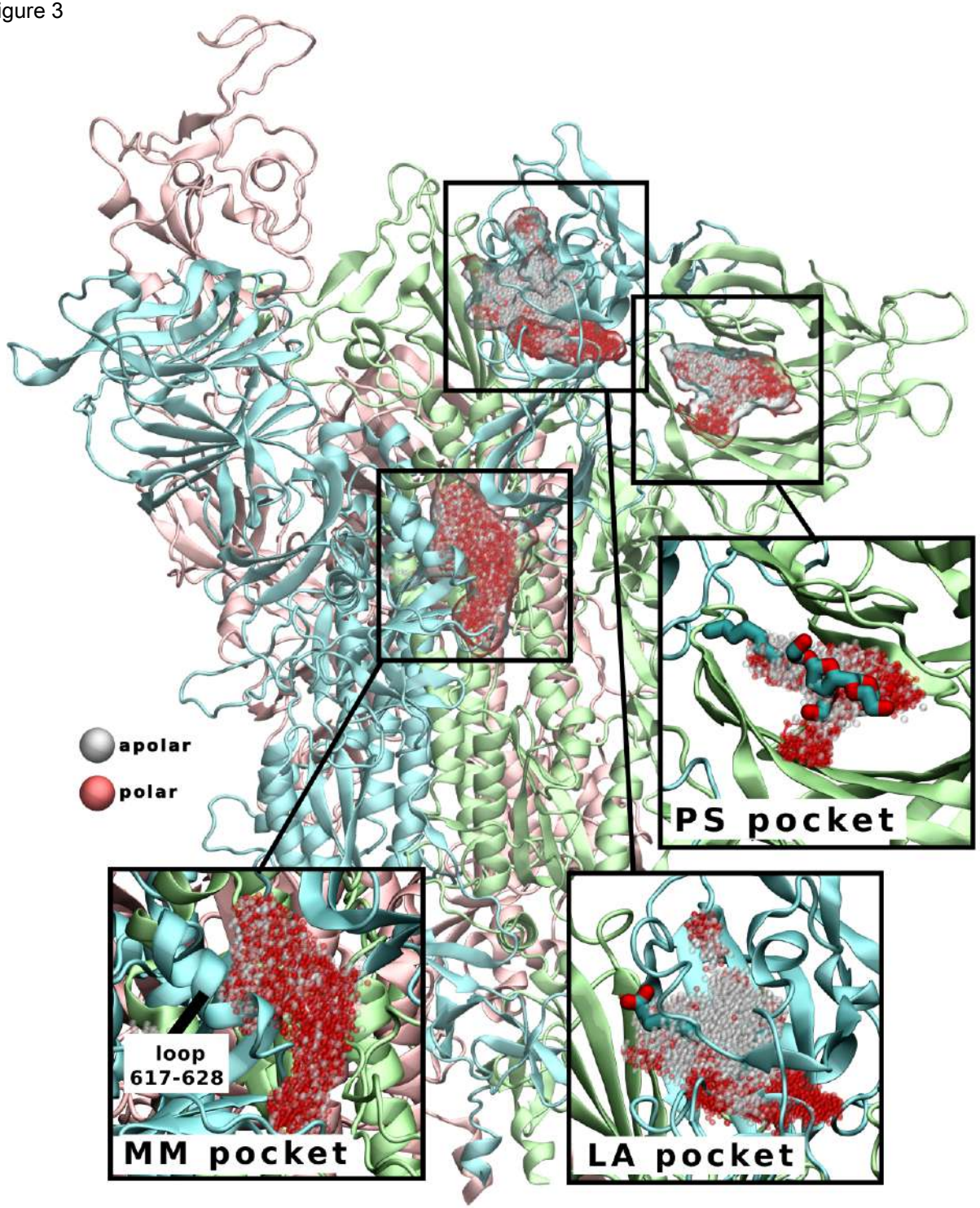

Figure 4

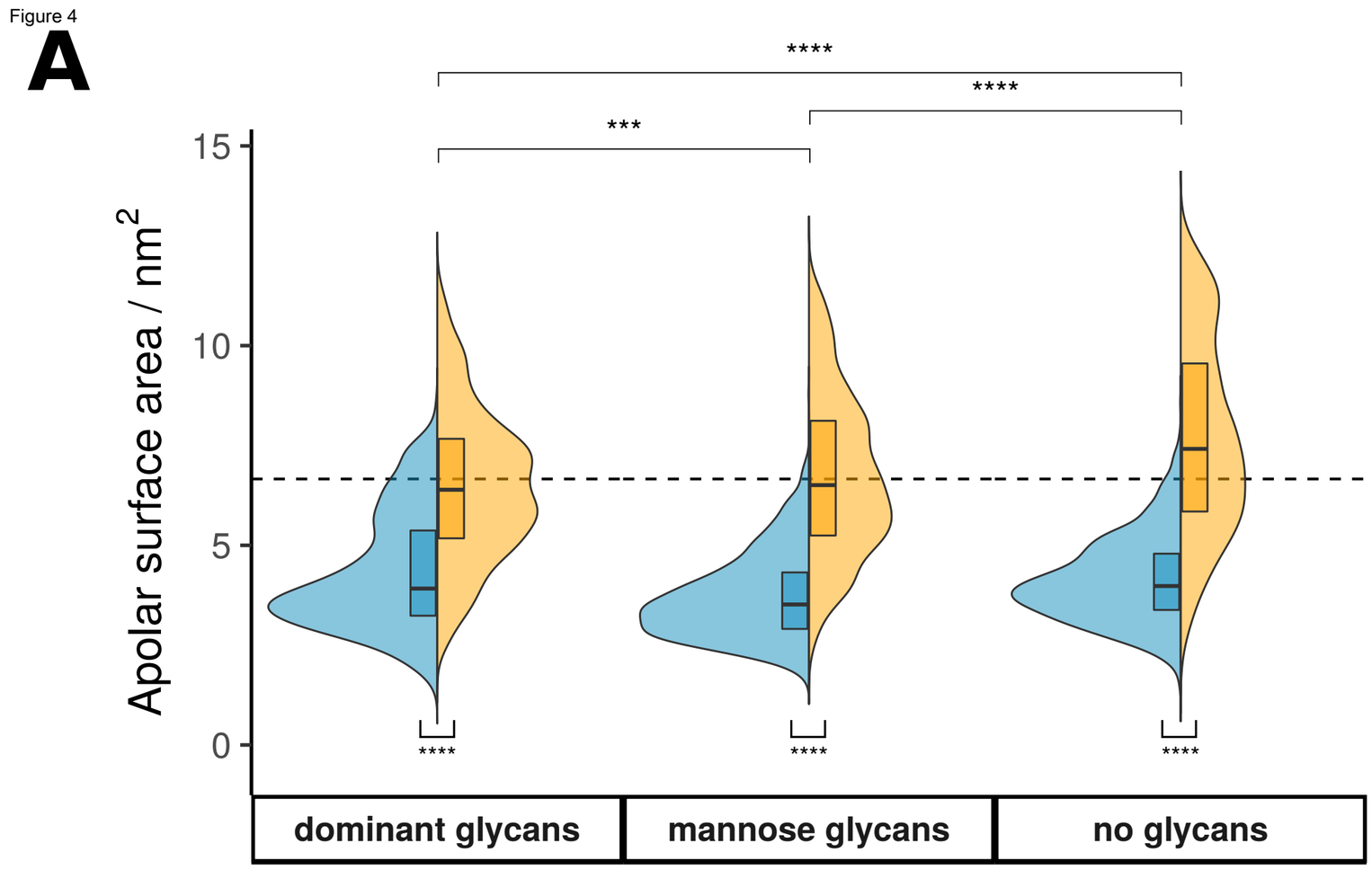
A
****
****
***
Apolar surface area / nm2
15
10
5
0
****
****
****
dominant glycans
mannose glycans
no glycans

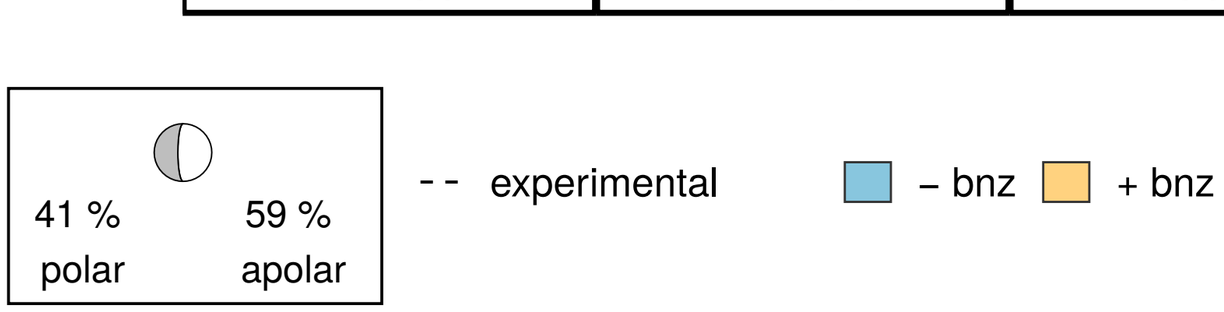
41 %
polar
59 %
apolar
experimental
– bnz
+ bnz

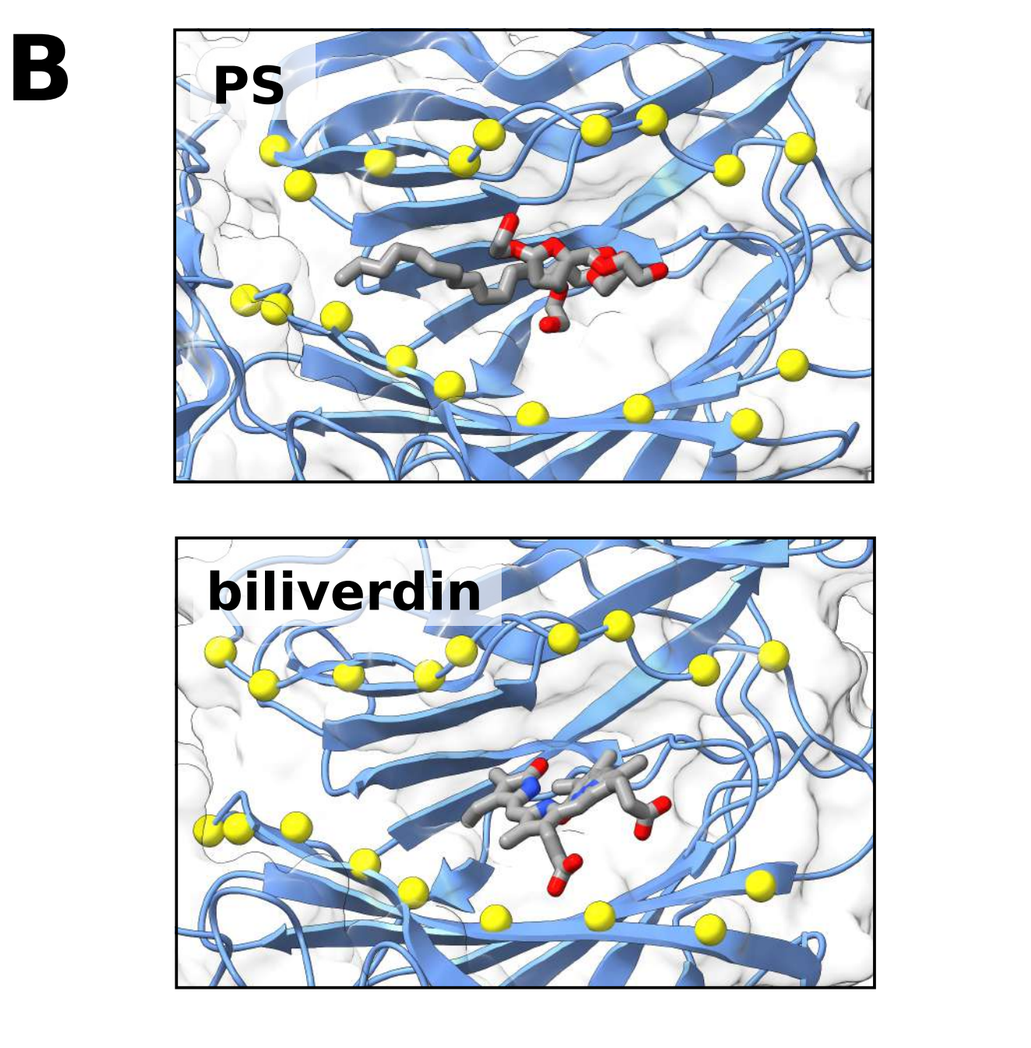
B
PS
biliverdin
benzene

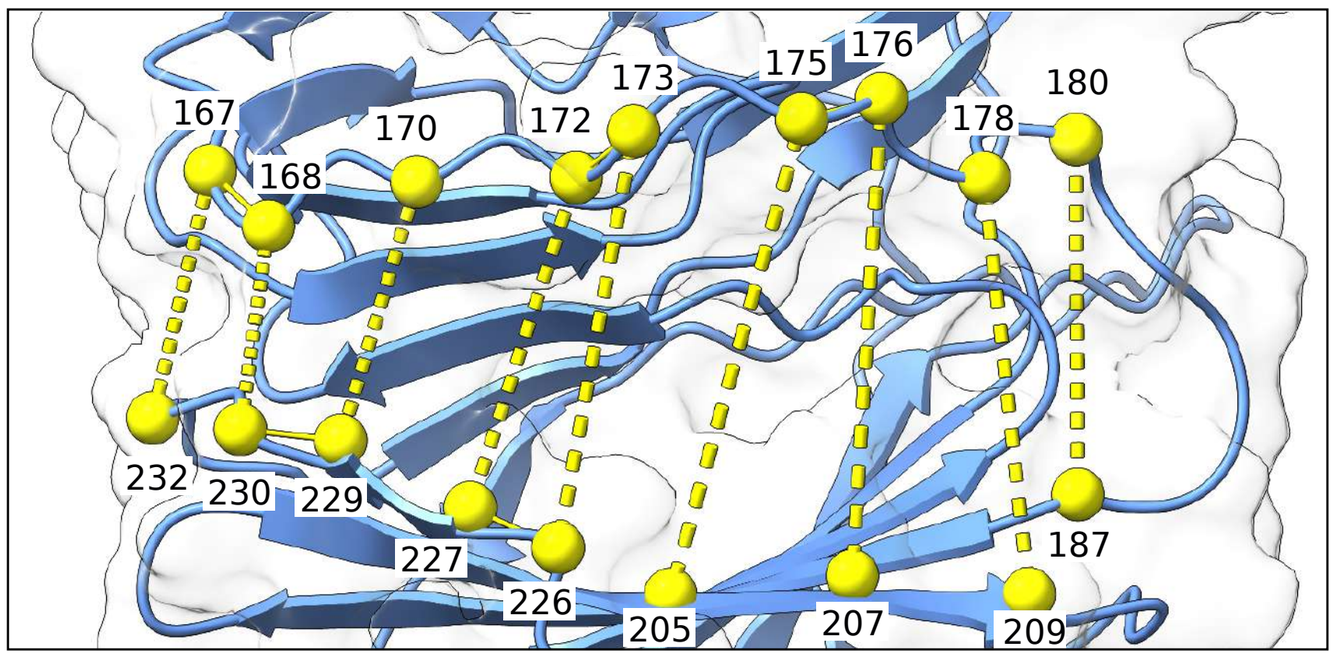
C
167
168
170
172
173
175
176
178
180
232
230
229
227
226
205
207
187
209

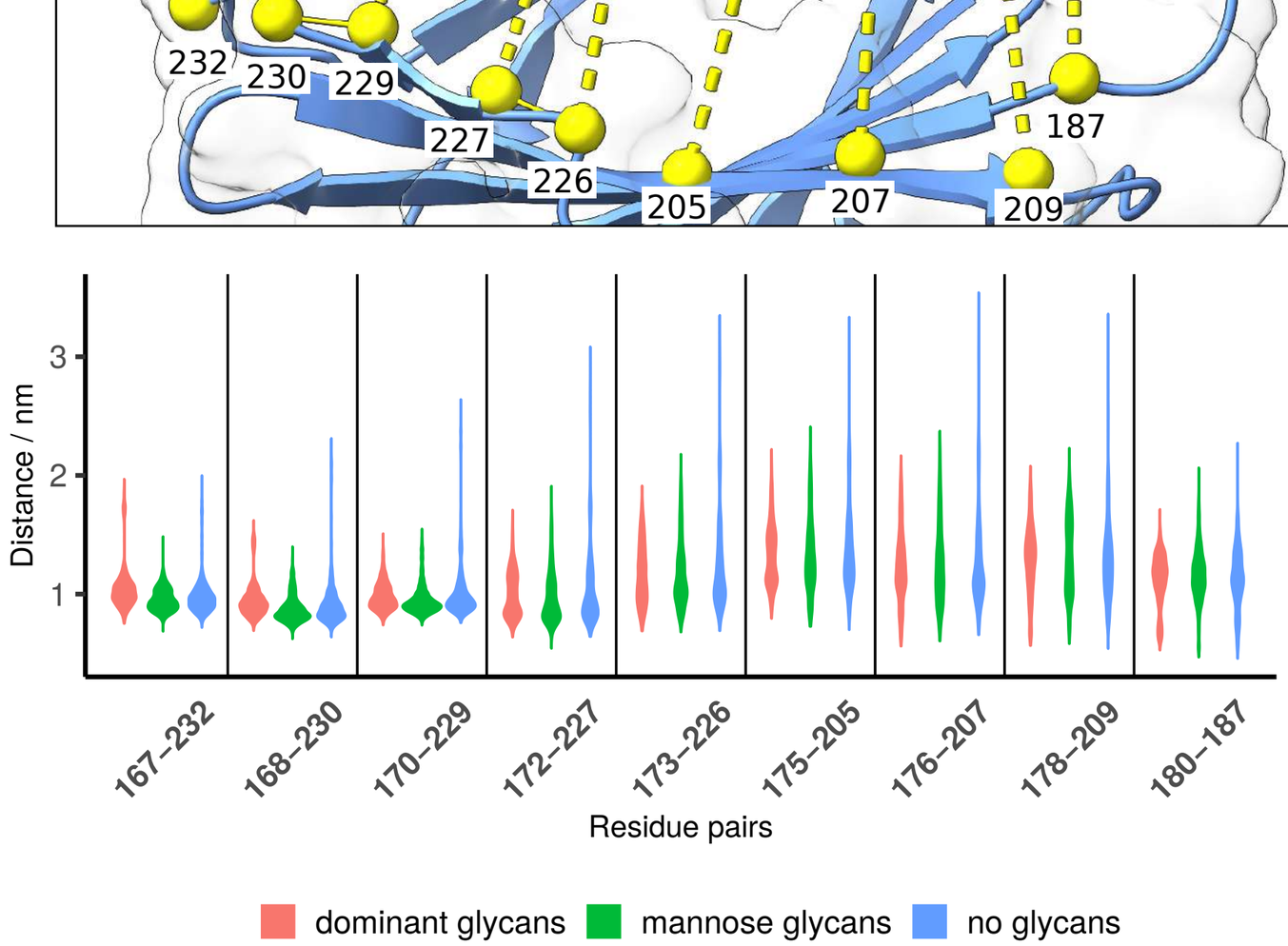
Distance / nm
3
2
1
167–232
168–230
170–229
172–227
173–226
175–205
176–207
178–209
180–187
Residue pairs
dominant glycans
mannose glycans
no glycans

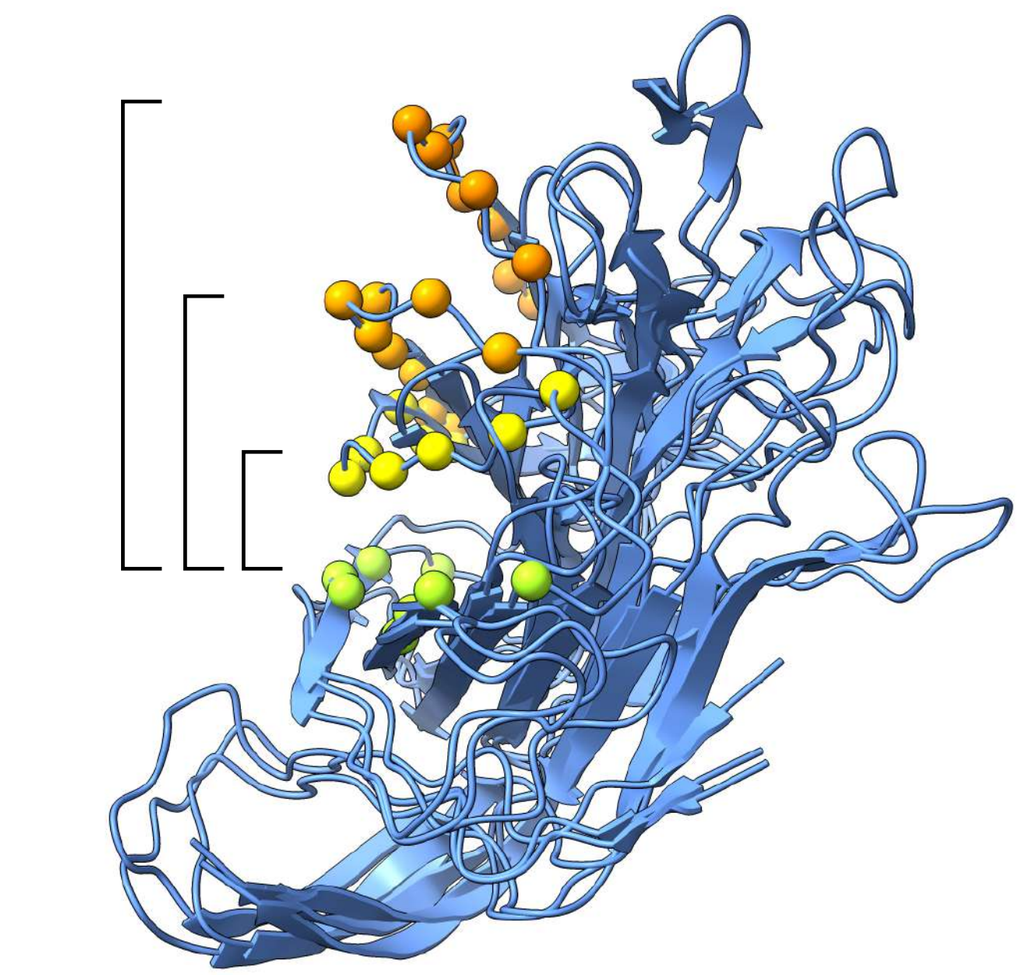
D

Figure 5

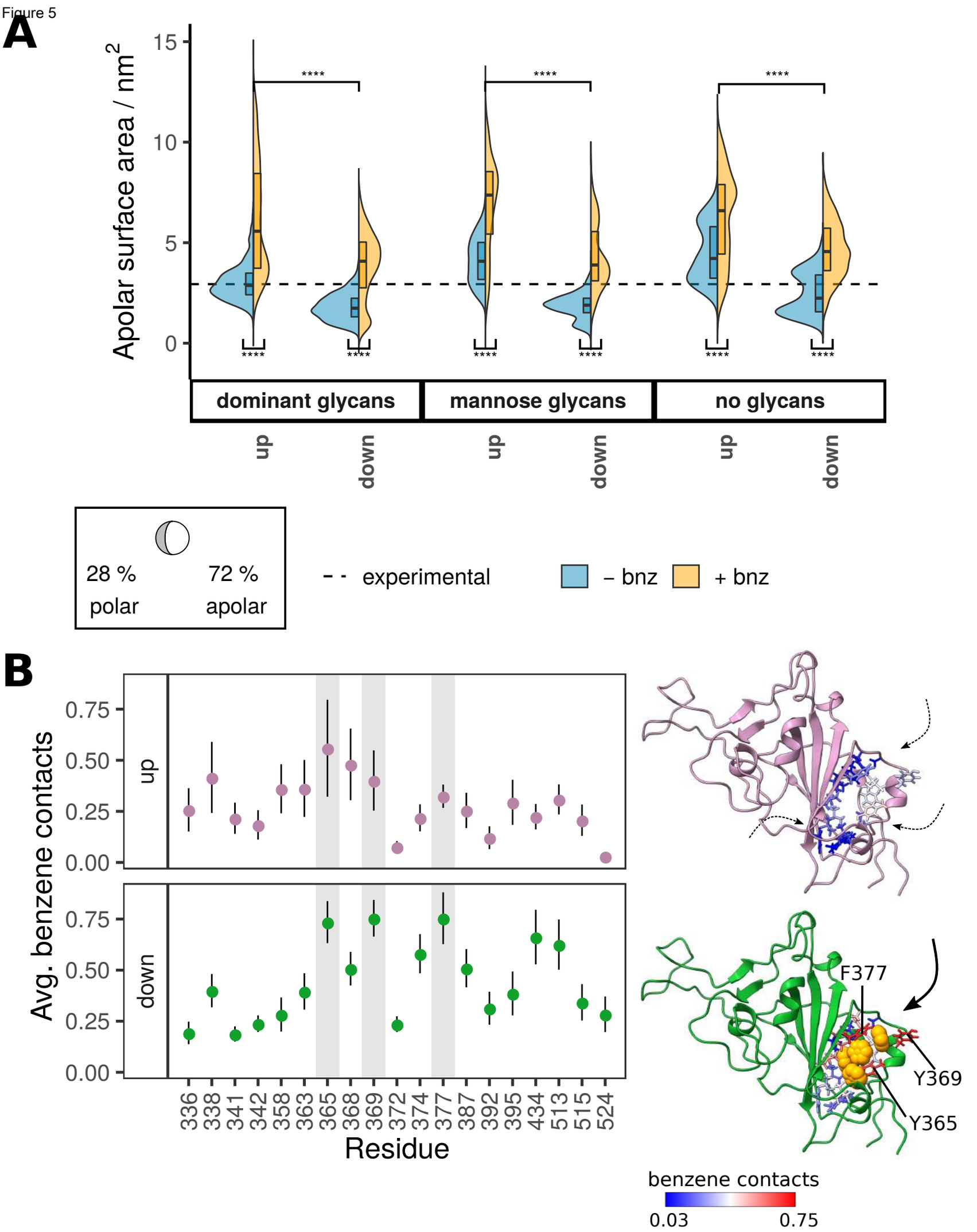
A
Apolar surface area / nm2
15
10
5
0
****
dominant glycans
mannose glycans
no glycans
up
down
28 %
polar
72 %
apolar
experimental
– bnz
+ bnz
B
Avg. benzene contacts
0.75
0.50
0.25
0.00
336
338
341
342
358
363
365
368
369
372
374
377
387
392
395
434
513
515
524
Residue
F377
Y369
Y365
benzene contacts
0.03
0.75

Figure 6

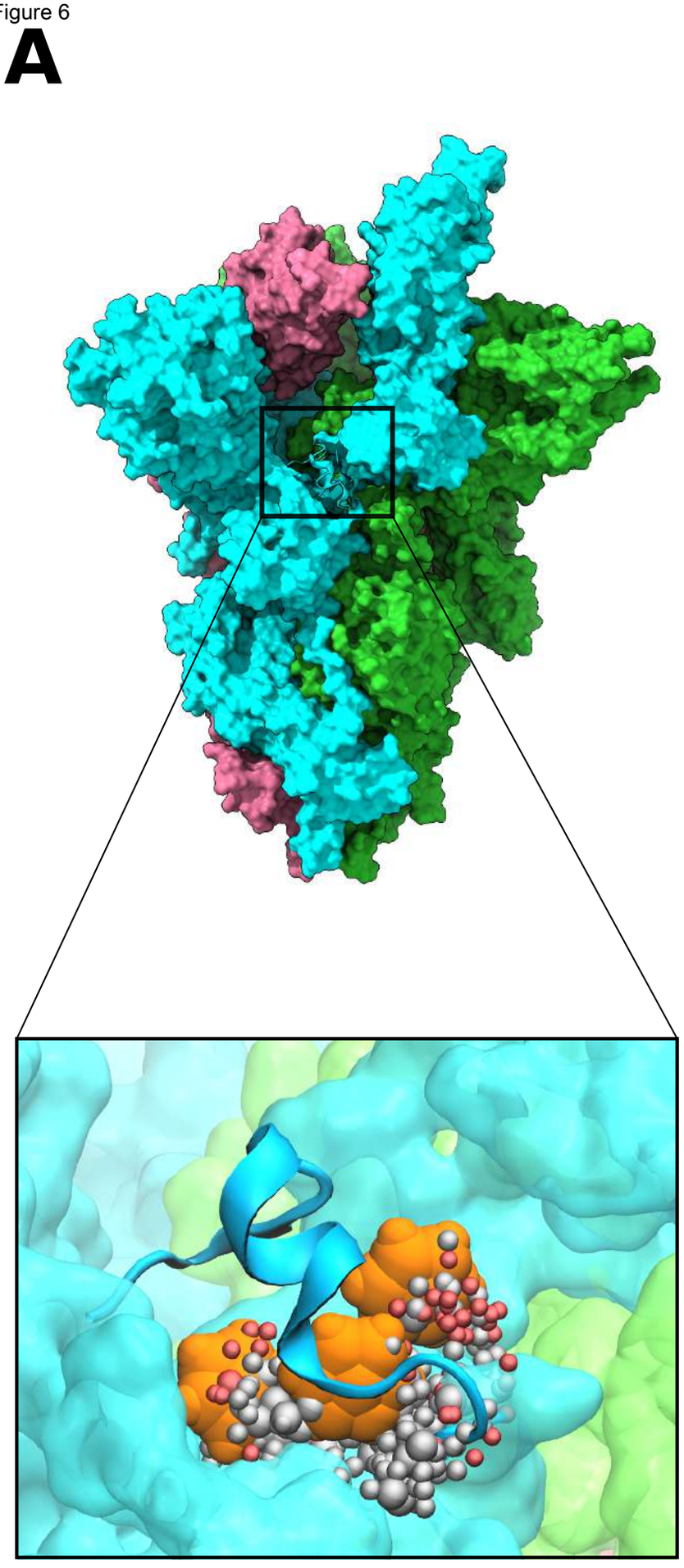
A
B
Apolar surface area / nm^2
20
15
10
5
****
**
dominant glycans
mannose glycans
no glycans
up
down
50 %
polar
50 %
apolar
– bnz
+ bnz
C
617-628 loop
up
down
avg. glycan contacts
0
6.9

Figure 7

Peptide 617 - 632
CTEVPVAIHADQLTPT

Experiment - S protein

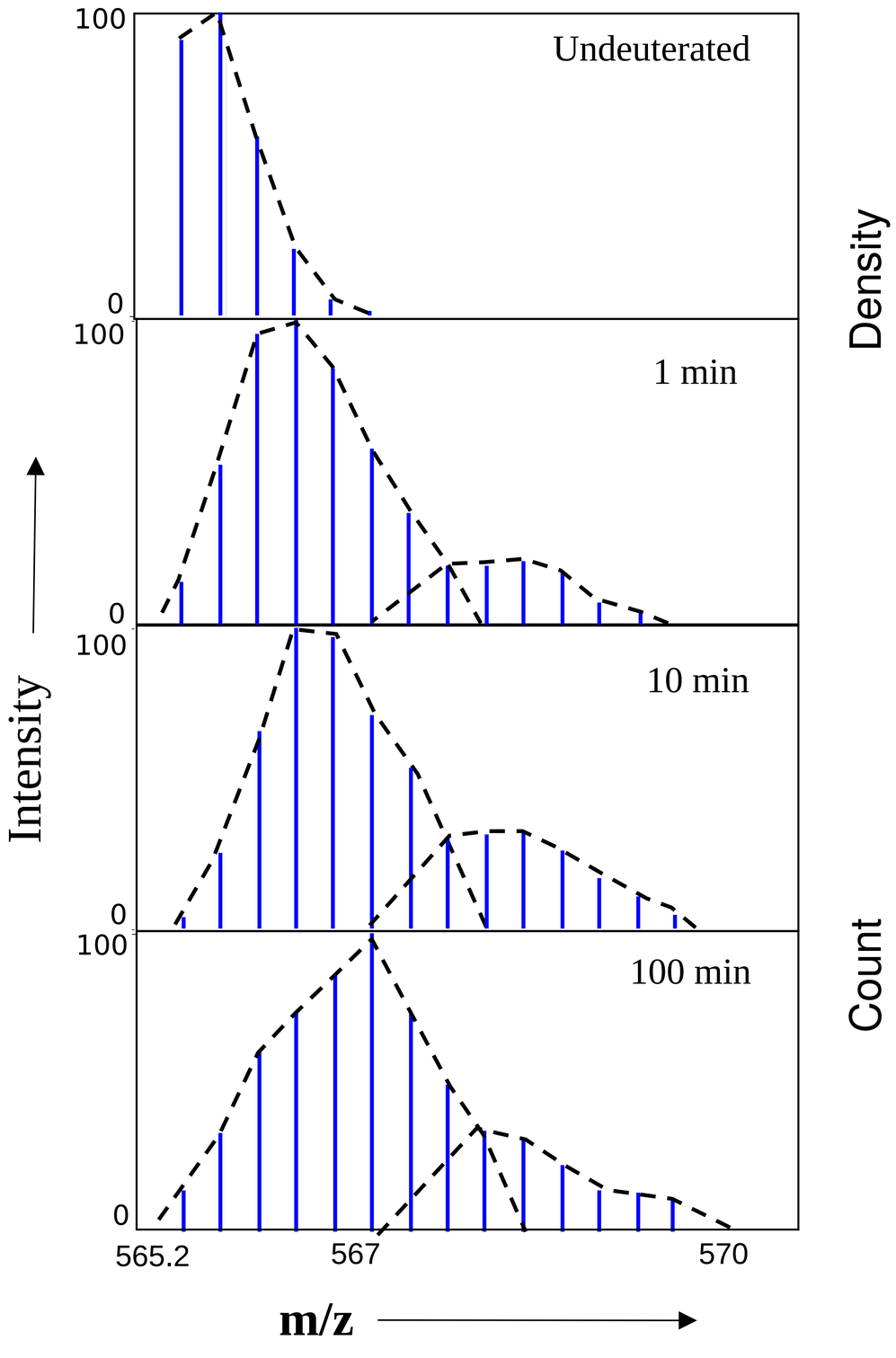

Simulation

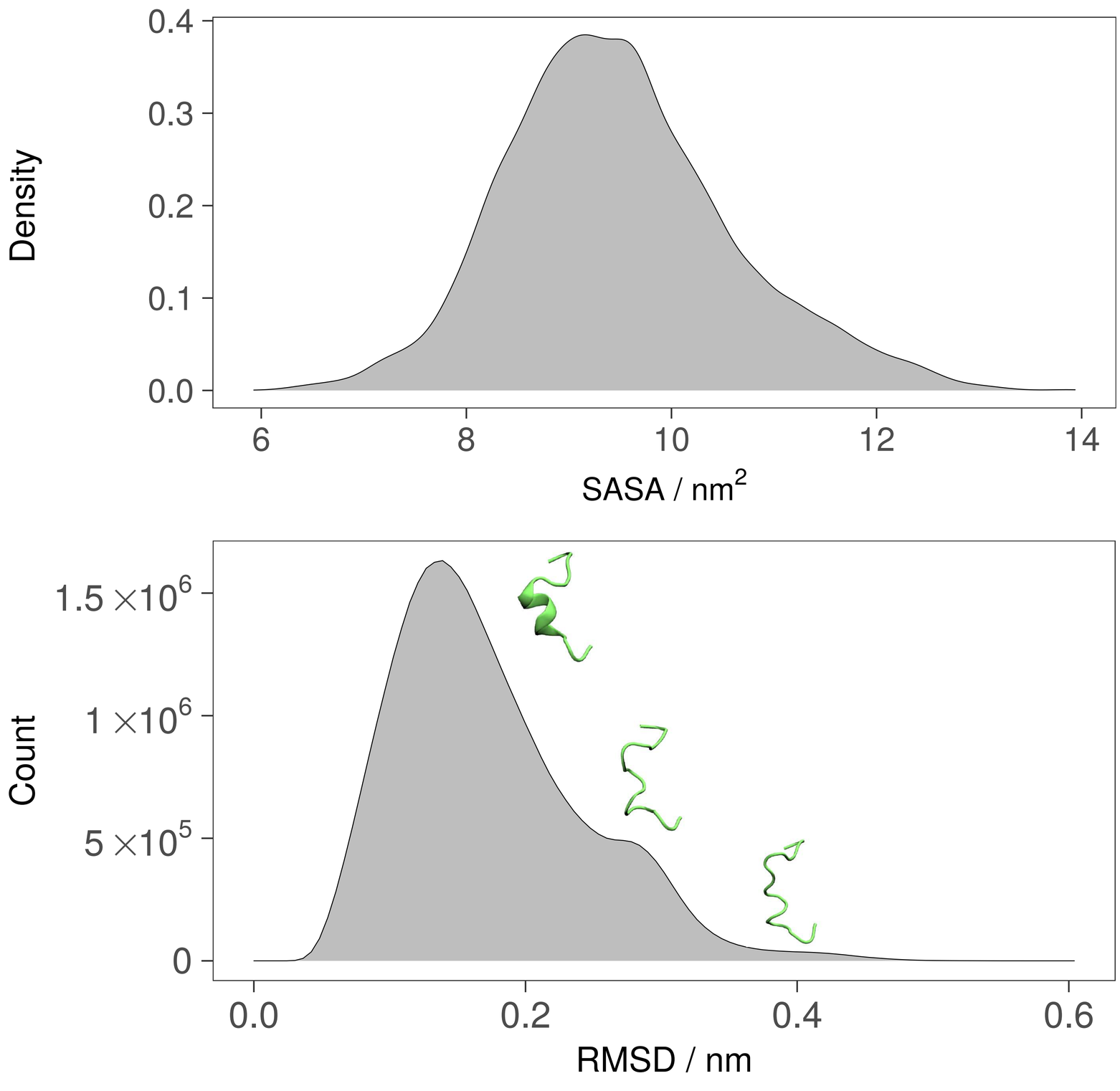

KEY RESOURCES TABLE

REAGENT or RESOURCE	SOURCE	IDENTIFIER
Chemicals, peptides, and recombinant proteins		
Deuterium oxide (chemical)	Cambridge Isotope Laboratories	CAS# 7789-20-0
Tris(2-carboxyethyl) phosphine-hydrochloride (TCEP-HCl)	Sigma-Aldrich	51805-45-9
GnHCl	Sigma-Aldrich	50-01-1
Phosphate buffer saline tablets	Sigma-Aldrich	Product No.: P4417-50TAB
Deposited data		
SARS-CoV-2 genome	Wu et al., 2020	GenBank: MN908947
SARS-CoV-2 S ECD open state	Wrapp et al., 2020	PDB: 6VSB
SARS-CoV-2 S RBD bound to ACE2	Yan et al, 2020	PDB: 6M17
SARS-CoV-2 S ECD closed state	Cai et al, 2020	PDB: 6XR8
SARS-CoV HR2	Hakansson-McReynolds et al., 2020	PDB: 2FXP
HIV-1 gp-41 TM	Dev et al., 2016	PDB: 5JYN
SARS-CoV-2 S model dominant glycans	This work	https://doi.org/10.5281/zenodo.5760159
SARS-CoV-2 S model mannose glycans	This work	https://doi.org/10.5281/zenodo.5760159
SARS-CoV-2 S model no glycans	This work	https://doi.org/10.5281/zenodo.5760159
SARS-CoV-2 S ECD dominant glycans after benzene simulations	This work	https://doi.org/10.5281/zenodo.5760159
SARS-CoV-2 S ECD mannose glycans after benzene simulations	This work	https://doi.org/10.5281/zenodo.5760159
SARS-CoV-2 S ECD no glycans after benzene simulations	This work	https://doi.org/10.5281/zenodo.5760159
HDX data	Raghuvamsi et.al., 2021	ProteomeXchange Consortium: PXD23138
Experimental models: Cell lines		
Human embryonic kidney (HEK293-6E)	NRC, Canada	RRID:CVCL_HF20
Oligonucleotides		
S protein gene of SARS-CoV-2 (1–1208)	Twist Biosciences, Singapore	QHD43416.1
Recombinant DNA		
pTT5 expression vector (plasmid)	Addgene, USA	RRID:Addgene_52367
Software and algorithms		
Modeller v9.21	Sali and Blundell, 1994	https://salilab.org/modeller/
PSIPRED 4.0	Jones, 1989	http://bioinf.cs.ucl.ac.uk/psipred/
CHARMM-GUI Membrane Builder	Lee et al., 2019	https://www.charmm-gui.org
GROMACS 2018	Abraham et al., 2015	https://www.gromacs.org
VMD 1.9	Humphrey and Dalke, 1996	https://www.ks.uiuc.edu/Research/vmd/

UCSF ChimeraX 1.2.5	Pettersen et al, 2021	https://www.rbvi.ucsf.edu/chimerax/
MDPocket	Schmidtke et al, 2011	http://fpocket.sourceforge.net/
Consurf	Ashkenazy et al., 2016	https://consurf.tau.ac.il
DynamX	Waters Corporation (Milford MA)	DynamX version 3.0
ProteinLynx Global Server	Waters Corporation (Milford MA)	PLGS version 3.0.1

Uncovering cryptic pockets in the SARS-CoV-2 spike glycoprotein – Supplemental Information

Lorena Zuzic,[1,2,†] Firdaus Samsudin,[1,†] Aishwary T. Shivgan,[1] Palur V. Raghuvamsi,[3] Jan K. Marzinek,[1] Alister Boags,[1,4] Conrado Pedebos,[4,5] Nikhil K. Tulsian[3,6], Jim Warwicker,[7] Paul MacAry[8], Max Crispin,[9] Syma Khalid,[4,5,*] Ganesh S. Anand[3,10,*] and Peter J. Bond[1,3,‡,*]

[1]Bioinformatics Institute (A*STAR), Singapore 138671, Singapore
[2]Department of Chemistry, Faculty of Science and Engineering, Manchester Institute of Biotechnology, The University of Manchester, Manchester M1 7DN, United Kingdom
[3]Department of Biological Sciences, National University of Singapore, Singapore 117543, Singapore
[4]School of Chemistry, University of Southampton, Southampton SO17 1BJ, United Kingdom
[5]Department of Biochemistry, University of Oxford, Oxford OX1 3QU, United Kingdom
[6]Department of Biochemistry, National University of Singapore, Singapore 117546, Singapore
[7]School of Biological Sciences, Faculty of Biology, Medicine and Health, Manchester Institute of Biotechnology, The University of Manchester, Manchester M1 7DN, United Kingdom
[8]Life Sciences Institute, Centre for Life Sciences, National University of Singapore, 28 Medical Drive, Singapore 117546, Singapore
[9]School of Biological Sciences, University of Southampton, Southampton SO17 1BJ, United Kingdom
[10]Department of Chemistry, The Pennsylvania State University, University Park, PA 16802, United States of America

[†]These authors contributed equally to the paper
[‡]Lead contact

*To whom correspondence should be addressed:
E-mail: peterjb@bii.a-star.edu.sg **(Lead Contact)**
E-mail: gsa5089@psu.edu
E-mail: s.khalid@soton.ac.uk

Table S1: List of simulations (related to Star Methods)

S protein glycosylation state	Benzene concentration (M)	Simulation time (ns)	Number of replicates
Non-glycosylated	0	200	2
High mannose	0	200	2
Dominant glycans	0	200	2
Non-glycosylated	0.2	200	3
High mannose	0.2	200	3
Dominant glycans	0.2	200	3
Dominant glycans ECD only	0.2	200	3

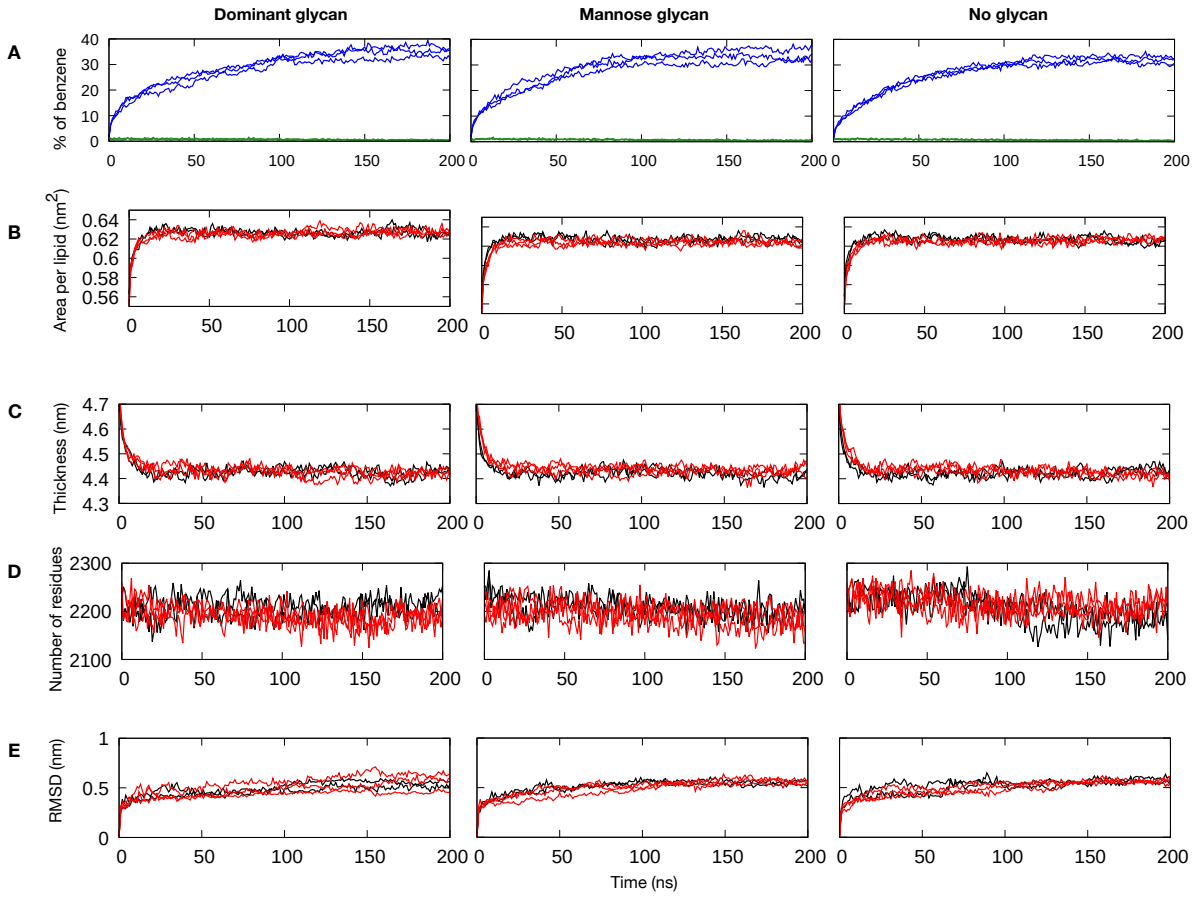

Figure S1: Membrane and protein structural properties during simulations of S protein with and without benzene (related to Figure 1). (A) Percentage of benzene in contact with the membrane lipids (green) or S protein (blue) throughout the simulations with benzene. Cut-off for contact is 0.4 nm. **(B), (C)** Area per lipid and membrane thickness in simulations with (red) and without benzene (black). **(D)** Total number of residues with secondary structural elements (α-helix, β-sheet, β-bridge and turn). **(E)** Backbone RMSDs for the ECD (residue 27-1146).

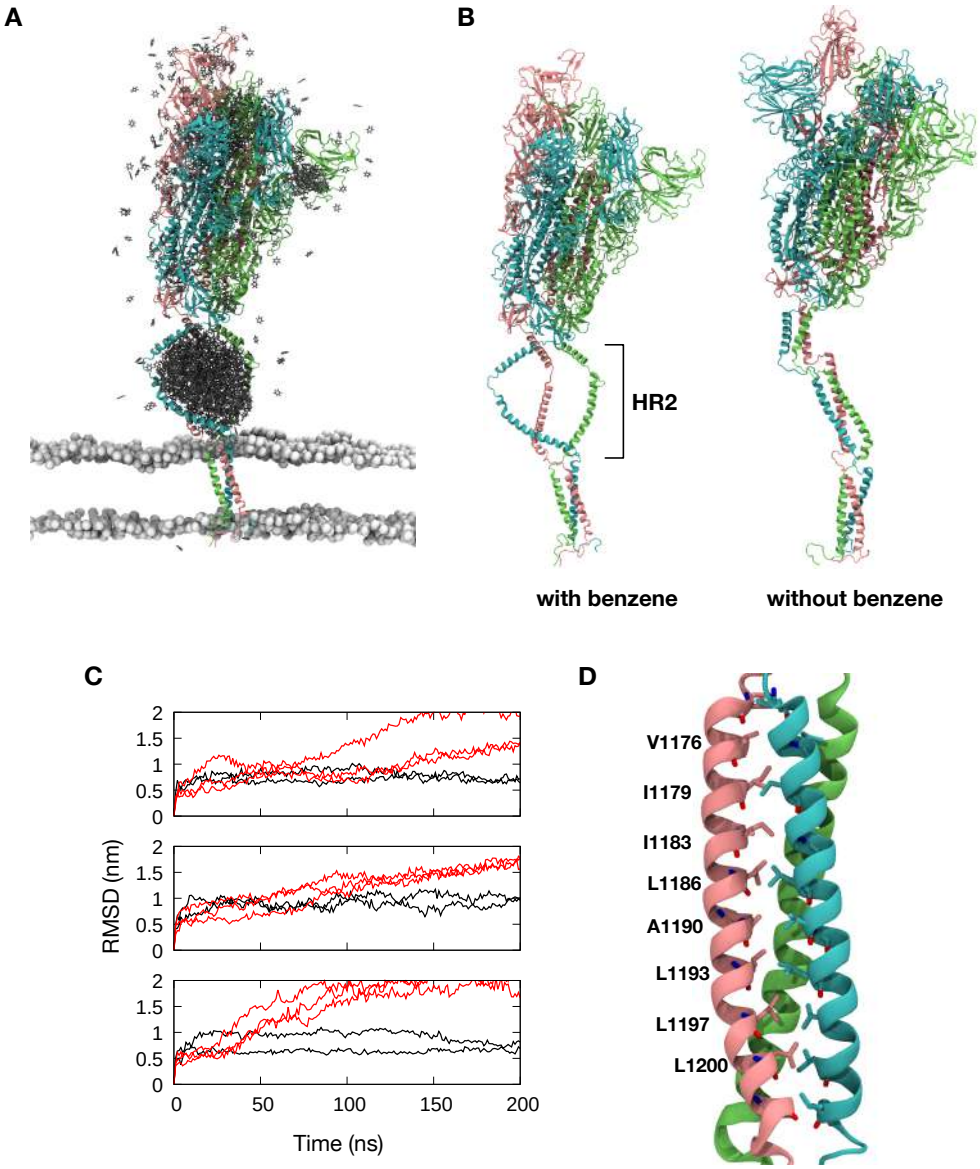

Figure S2: Aggregation of benzene around the HR2 domain (related to Figure 1). (A) The final snapshot from one of the simulations of glycosylated S protein open state with 0.2 M benzene. Benzene is shown in stick representation and coloured grey. For clarity, only benzene found within 2.0 nm of the protein is shown. **(B)** Comparison of protein structures at the end of simulations with and without benzene. HR2 domain is labelled. **(C)** Backbone RMSDs for the HR2 domain from simulations with (red) and without benzene (black). Dominant glycans (top); mannose glycans (middle); no glycans (bottom). **(D)** Hydrophobic residues at the interface of the HR2 domain.

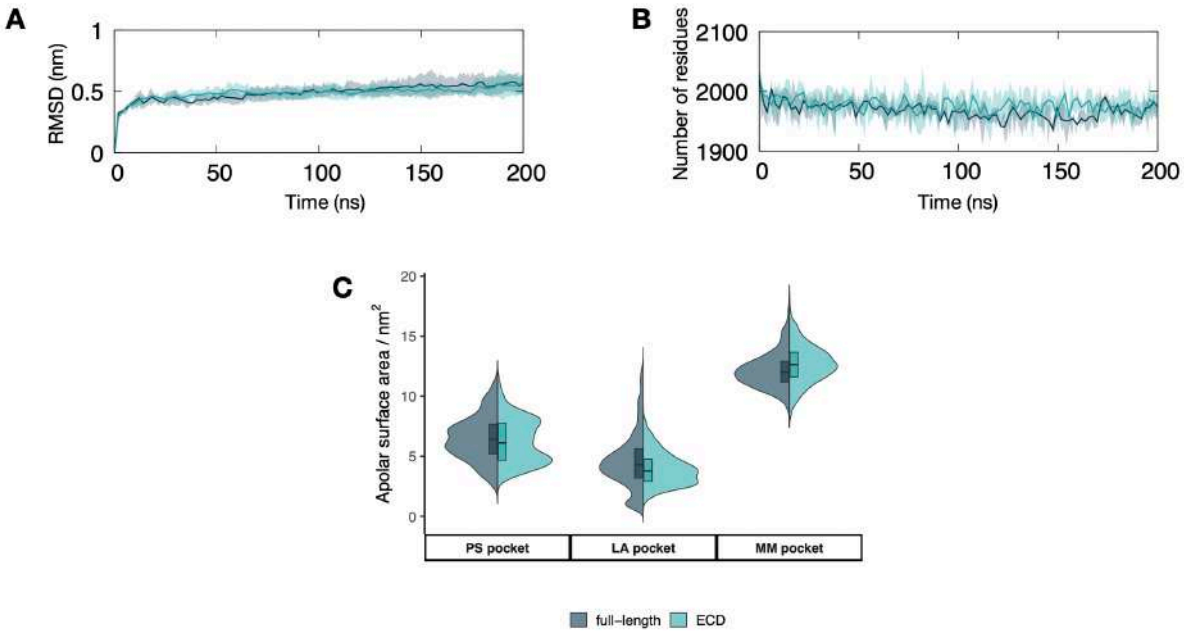

Figure S3: Comparison of simulations with benzene of full-length S protein versus ECD only (related to Figure 1). (A) Backbone RMSDs for the ECD from simulations of isolated ECD dominant glycans (green) and full-length S protein dominant glycans (black). (**B**) Total number of residues with secondary structural elements (α-helix, β-sheet, β-bridge and turn). **(C)** Apolar surface area of the pockets described in Figure 3 calculated from both sets of simulations.

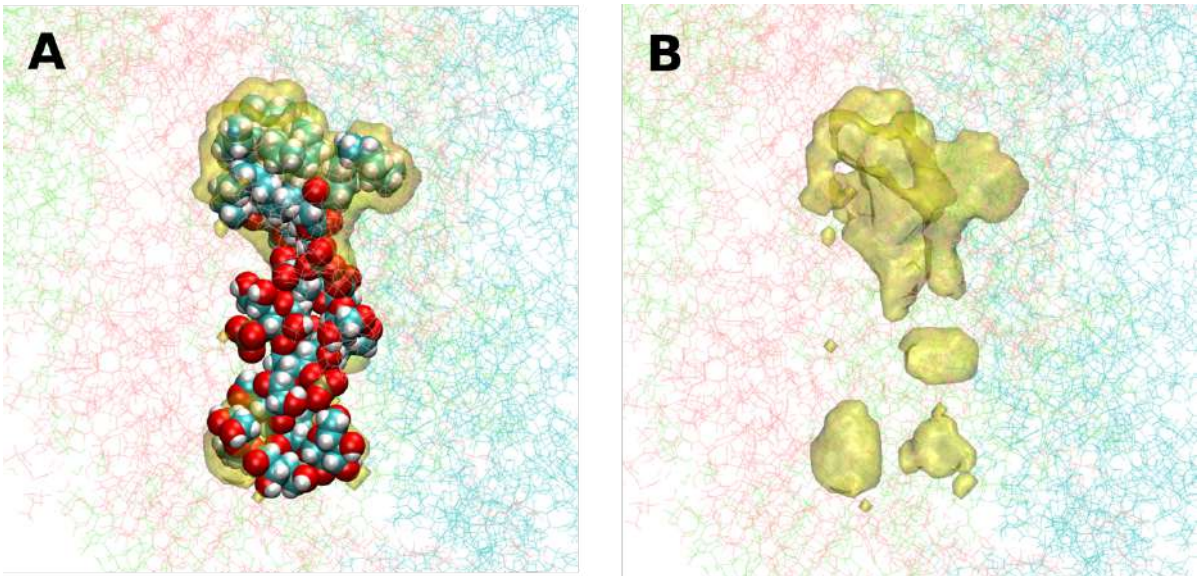

Figure S4: Location and properties of proposed LPS pocket (related to Figure 3). LPS pocket is defined as any pocket area within 0.2 nm of the LPS molecule. **(A)** LPS molecule shown in spheres docked on a previously proposed LPS pocket (Petruk et al., 2021). Mapped pocket area is shown as yellow surface. LPS pocket predominantly outlines the fatty acid tail portion of the LPS, while the hydrophilic sugar components are largely outside any detected pocket regions. **(B)** The outline of the LPS pocket without a bound ligand.

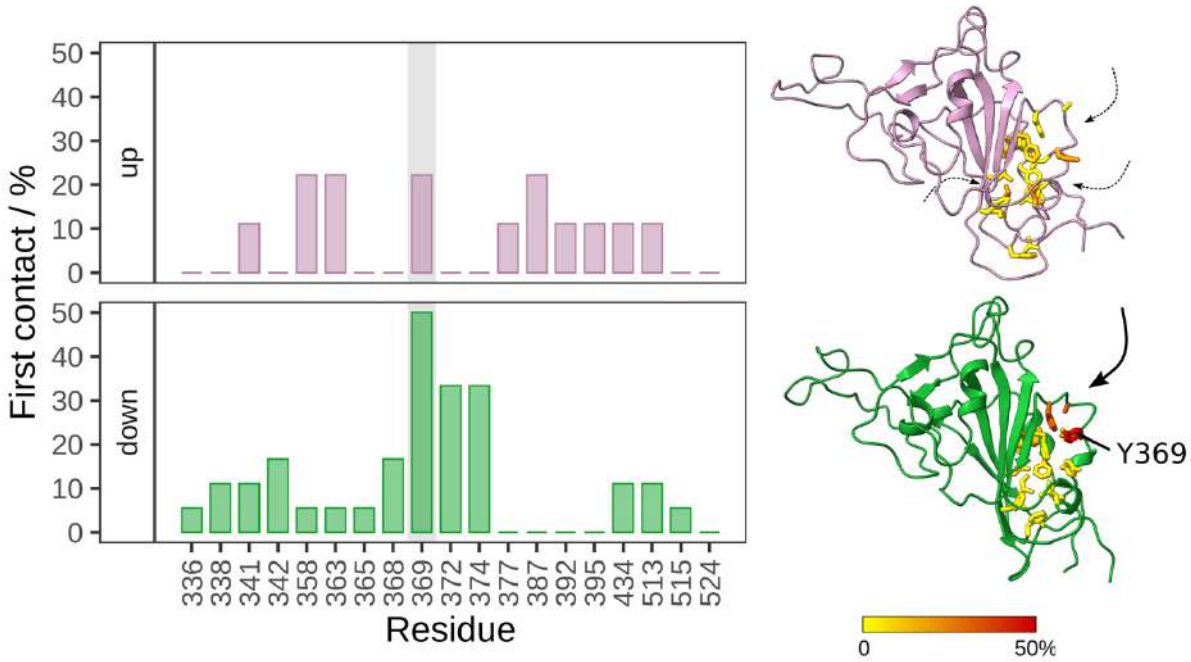

Figure S5. The first point of contact for benzene probes entering the LA pocket and likely ligand entry routes, as shown with arrows (related to Figure 5). The first contact is expressed as a percentage of simulations in which the residue in question establishes initial contact with the ligand, thus marking the entry route for benzene. The highest contact residue, Tyr369, is highlighted in grey on the plot and labelled on the structure. The RBD structures are shown in ribbon representation – 'up' in purple and 'down' in green. LA pocket residues are displayed as sticks and coloured according to the first contact frequency. Down conformation presents a single entry route for the ligands, whereas the up conformation cannot offer a single determinate mode of binding.

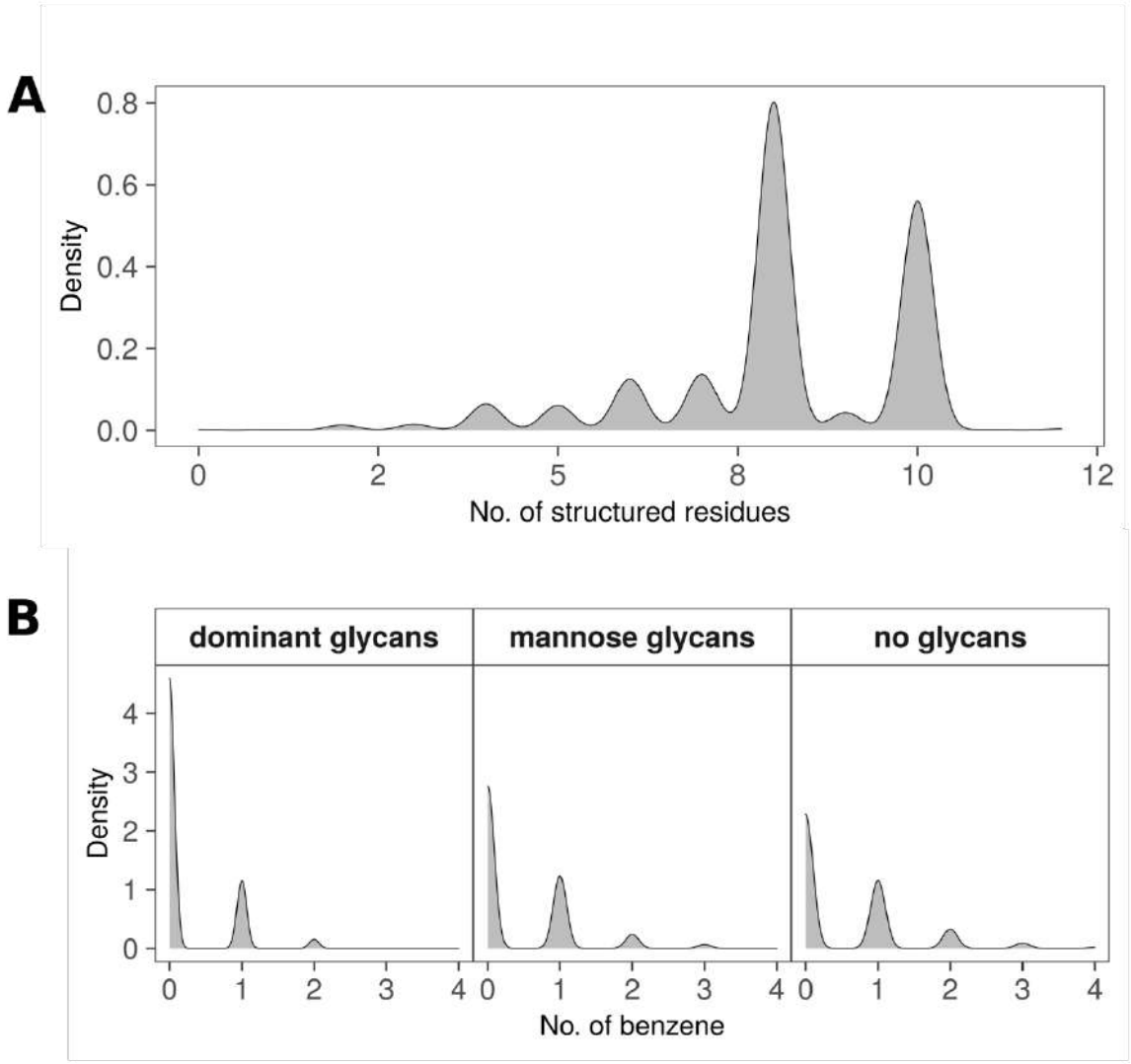

Figure S6: Properties of MM pocket segment (related to Figure 6). (A) Cumulative density distribution of number of residues in the 617-628 loop that are structured (either as α-helix or turn). **(B)** Number of benzene molecules that occupy a segment of the MM pocket underneath the 617-628 loop (see Figure 6A). The maximum number of benzenes occupying the pocket at any given point was three.

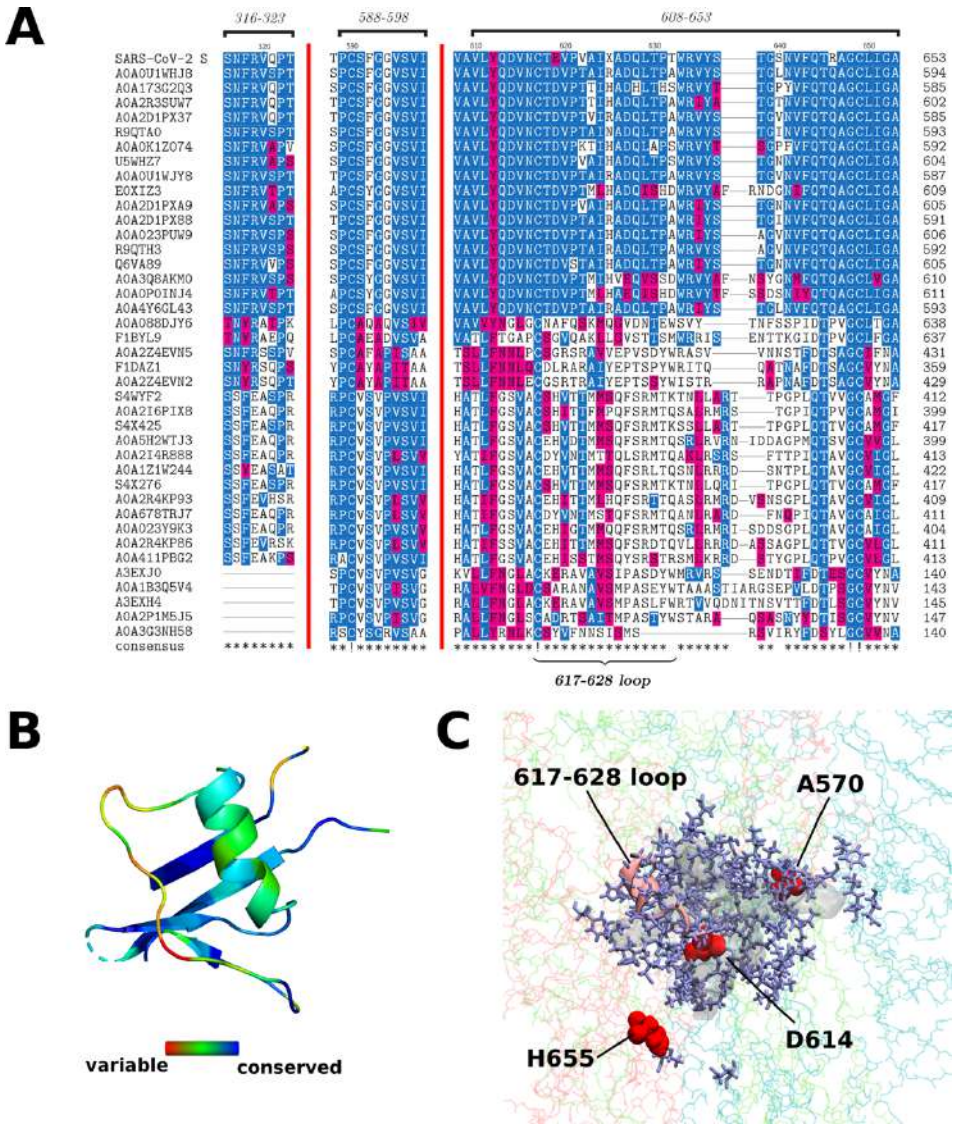

Figure S7: Conservation of the MM pocket segment underneath the 617-628 loop (related to Figure 6). Sequences were selected and scored using CONSURF webserver (details in Methods). **(A)** Multiple sequence alignment of the MM pocket segment. Residues are shaded based on similarity, using a threshold of 30%. **(B)** MM pocket segment is shown in cartoon representation and is coloured according to CONSURF score. **(C)** The MM pocket is shown in transparent surface representation, residues surrounding the pocket are shown in licorice, and the 617-628 loop in cartoon. The remainder of the S protein is shown in pink, cyan, and lime lines. Residues close to the MM pocket and mutated in novel SARS-CoV-2 strains are shown in red spheres.